The Detection, Genesis, and Modeling of Turbulence Intermittency in the Stable Atmospheric Surface Layer

MOHAMMAD ALLOUCHE,[a] ELIE BOU-ZEID,[a] CEDRICK ANSORGE,[b] GABRIEL G. KATUL,[c] MARCELO CHAMECKI,[d]
OTAVIO ACEVEDO,[e] SHAM THANEKAR,[f] AND JOSE D. FUENTES[f]

[a] *Department of Civil and Environmental Engineering, Princeton University, Princeton, New Jersey*
[b] *Institute of Geophysics and Meteorology, University of Cologne, Cologne, Germany*
[c] *Department of Civil and Environmental Engineering, Duke University, Durham, North Carolina*
[d] *Department of Atmospheric and Ocean Sciences, University of California, Los Angeles, Los Angeles, California*
[e] *Programa de Pós-Graduação em Meteorologia, Universidade Federal de Santa Maria, Santa Maria, Brazil*
[f] *Department of Meteorology and Atmospheric Sciences, The Pennsylvania State University, University Park, Pennsylvania*

(Manuscript received 23 February 2021, in final form 11 December 2021)

ABSTRACT: Intermittent transitions between turbulent and nonturbulent states are ubiquitous in the stable atmospheric surface layer (ASL). Data from two field experiments in Utqiaġvik, Alaska, and from direct numerical simulations are used to probe these state transitions so as to (i) identify statistical metrics for the detection of intermittency, (ii) probe the physical origin of turbulent bursts, and (iii) quantify intermittency effects on overall fluxes and their representation in closure models. The analyses reveal three turbulence regimes, two of which correspond to weakly turbulent periods accompanied by intermittent behavior (regime 1: intermittent; regime 2: transitional), while the third is associated with a fully turbulent flow. Based on time series of the turbulence kinetic energy (TKE), two nondimensional parameters are proposed to diagnostically categorize the ASL state into these regimes; the first characterizes the weakest turbulence state, while the second describes the range of turbulence variability. The origins of intermittent turbulence activity are then investigated based on the TKE budget over the identified bursts. While the quantitative results depend on the height, the analyses indicate that these bursts are predominantly advected by the mean flow, produced locally by mechanical shear, or lofted from lower levels by turbulent ejections. Finally, a new flux model is proposed using the vertical velocity variance in combination with different mixing length scales. The model provides improved representation (correlation coefficients with observations of 0.61 for sensible heat and 0.94 for momentum) compared to Monin–Obukhov similarity (correlation coefficients of 0.0047 for sensible heat and 0.49 for momentum), thus opening new pathways for improved parameterizations in coarse atmospheric models.

SIGNIFICANCE STATEMENT: Airflow in the lowest layer of the atmosphere is often modulated by a strong gradient of temperature when the surface is much cooler than the air. Such a regime results in weak turbulence and mixing, and is ubiquitous during nighttime and in polar regions. Understanding and modeling atmospheric flow and turbulence under such conditions are further complicated by "turbulence intermittency," which manifests as periods of strong turbulent activity interspersed in a more quiescent airflow. The turbulent periods dominate the air–surface exchanges even when they occur over a small fraction of the time. This paper develops approaches to detect and classify such intermittent regimes, examines how the turbulent bursts are generated and advected, and offers guidance on representing such regimes in geophysical models. The findings have the potential to advance weather forecasting and climate modeling, particularly in the all-important polar regions.

KEYWORDS: Arctic; Turbulence; Boundary layer; Buoyancy; Surface fluxes; Parameterization

1. Introduction

A stable atmospheric surface layer (ASL) develops when the surface is cooler than the air aloft, a condition widely observed during nighttime and more consequentially during polar winters with low insolation. The urge to elucidate the physics of surface–atmosphere exchanges in the stable polar ASL, and how best to model them, is underscored by polar amplification: polar regions have experienced the most rapid rate of environmental change over the past decade (Richter-Menge et al. 2017; Wendisch et al. 2017).

The structure of the stable ASL is determined by the interplay between static stability of the air and shear generation of turbulence kinetic energy (TKE). When the latter dominates, the ASL is generally described as weakly stable, whereas when the former dominates, it is described as strongly stable (Mahrt 1998, 1999; Stull 2008). A specific challenge for physical understanding and modeling is posed by the intermittent turbulence dynamics observed in the strongly stable regime (Fernando and Weil 2010). During such intermittent periods, turbulence observed by a fixed sensor becomes statistically unsteady as the balance between shear production and buoyant and viscous destructions varies in time (Mahrt et al. 2013; Shah and Bou-Zeid 2014, 2019; Katul et al. 2014; Mahrt and Bou-Zeid 2020). The corresponding spatial patterns reveal patches of turbulence interspersed in a quiescent flow (Ansorge and Mellado 2016). These bursting turbulent patches and periods may produce a disproportionate fraction

---

Corresponding author: Elie Bou-Zeid, ebouzeid@princeton.edu

DOI: 10.1175/JAS-D-21-0053.1

of the surface–atmosphere fluxes, as hypothesized by Nappo (1991), and are consequential for a range of practical applications including electromagnetic wave propagation (Wyngaard et al. 2001), air quality forecasting and atmospheric chemistry (Strong et al. 2002; Weil 2011), wind profile classification (Muschinski and Sullivan 2013), and weather and climate modeling (Svensson and Holtslag 2009; Sorbjan 2010; Huang and Bou-Zeid 2013; Huang et al. 2013).

Classic similarity approaches are mostly found adequate under weakly stable conditions: e.g., the Monin–Obukhov similarity theory (MOST) tested among others by Persson (2003), the local similarity theory proposed by Nieuwstadt (1984), or the theory based on the Dougherty–Ozmidov length scale proposed by Grachev et al. (2014). These similarity theories, however, often fail in the intermittent strongly stable ASL (Fernando and Weil 2010; Mahrt et al. 2013), characterized by aperiodic temporal and spatial transitions between turbulent and quasi-laminar states in which turbulence is locally damped at all scales (Mahrt 1999). We refer to this type of intermittency here as "local" intermittency. It is conceptually related to the global intermittency defined and studied by Mahrt (1999) and Ansorge and Mellado (2014, 2016), but we label it "local" to underline its limited spatiotemporal extent. However, it is distinct from the internal fine-scale dissipation intermittency (Pope 2000). Many open questions remain on the detection and classification of "local" intermittency, the physical origins of the turbulent bursts that break the quiescence of the flow, and how to parameterize the impact of these intermittent dynamics on the mean flow and fluxes. These questions frame the research objectives of the present paper.

Classification and detection of locally intermittent turbulence has been approached from various perspectives in the literature of stable ASLs. Most studies tend to identify three regimes, corresponding to those identified by Mahrt (1998) based on heat fluxes as a function of atmospheric stability (weakly stable, transitionally stable, and very stable). For example, Van de Wiel et al. (2003) also suggest three regimes broadly corresponding to those of Mahrt: the turbulent, intermittent, and radiative regimes. A practical question is then what describes the onset of, or transitions in between, these different turbulence states. Recently, the hockey-stick transition (HOST) was proposed as an operational method for delineating the three regimes based on the discriminating criterion of threshold values of the mean wind speed at a given level: weak turbulence regime (1) if the mean wind is less than a certain threshold value at that height, strong turbulence regime (3) if the mean wind exceeds the threshold, and moderate turbulence regime (2) when the turbulence strength oscillates between regimes 1 and 3 as the mean wind fluctuates across its threshold value (Sun et al. 2012). While the wind speed criterion threshold remains useful (Lan et al. 2019), it may not offer a universal classification since it is a dimensional quantity. Furthermore, even single nondimensional indicators, such as the gradient Richardson number, may lead to locally misleading classification of stability regimes (Vercauteren et al. 2019). The need for two dimensionless parameters was thus recently suggested to broadly capture the collapse of turbulence in a stratified plane Couette flow (Van Hooijdonk et al. 2018). This motivates the first part of the analysis (section 3), where we seek to answer the following question: What nondimensional statistical indicators could be used to detect and characterize intermittency?

Once the periods that display intermittency are identified, one can then focus on the detection and analysis of the turbulent bursts, which have been characterized by lifetimes that can extend up to 20 min (Nappo 1991). A primary focus of previous research has been on the triggering mechanisms that generate TKE in a predominantly quiescent very stable ASL flow, and whether these triggers are external or internal. External disturbances that can generate turbulence include mesoscale phenomena such as large-scale shear instabilities, gravity waves, submeso fluctuations and low-level jets (LLJs) (Sun et al. 2002, 2004; Banta et al. 2007; Cuxart et al. 2007; Cava et al. 2019), horizontal meandering of the mean flow (Anfossi et al. 2005), or even passage of clouds inducing radiative perturbations (Cava et al. 2004). With these external mechanisms, downward transport of turbulence from upper-level instabilities toward the surface (top-down) is favored over, or at least as likely as, near-surface production. On the other hand, internal triggering mechanisms could stimulate such bursting events due to enhanced shear near the surface (Durst 1933), due to internal interactions between turbulent mixing and the mean shear (Pardyjak et al. 2002; Fernando 2005) that may be of cyclic nature (Van der Linden et al. 2020), or due to the ability of turbulence to store turbulent potential energy and redistribute it to TKE (Ayet et al. 2020). Recent direct numerical simulations (DNS) of the stratified planetary boundary layer also reveal that truly global intermittency, where the turbulence is severely damped (but not completely) everywhere in the domain of interest, is a phenomenon inherent to the stable ASL (Ansorge and Mellado 2014, 2016; Shah and Bou-Zeid 2014, 2019). These studies indicate that turbulence regeneration can spontaneously occur in the flow (Rorai et al. 2014), probably from the growth of the weak perturbations that persist, and does not require any external large-scale triggering mechanisms. Such internal mechanisms, either with local or global intermittency, would be expected to originate near the wall and would hence favor upward transport from lower-level instabilities (bottom-up). Both external and internal mechanisms might act simultaneously, with bursting events occurring over a range of temporal and spatial scales, which has hindered the ability to define the controlling mechanisms or processes behind the genesis of these bursts (Coulter and Doran 2002). This challenge motivates the second question of this paper discussed in sections 4 and 5: What are the origins of the turbulent bursts that enhance mixing and transport under intermittent and transitional regimes?

Finally, with these bursts identified and characterized, one may attempt to improve turbulence closure models for the highly stable intermittent periods using the uncovered physics. The turbulence closure literature is vast (see a recent review in Durbin 2018), and the specificities and details on how to include these closures in atmospheric numerical models are intricate (Stensrud 2007). But there is ample evidence that unsteady conditions pose particular challenges to classical closures in stable regimes (e.g., Huang et al. 2013), and

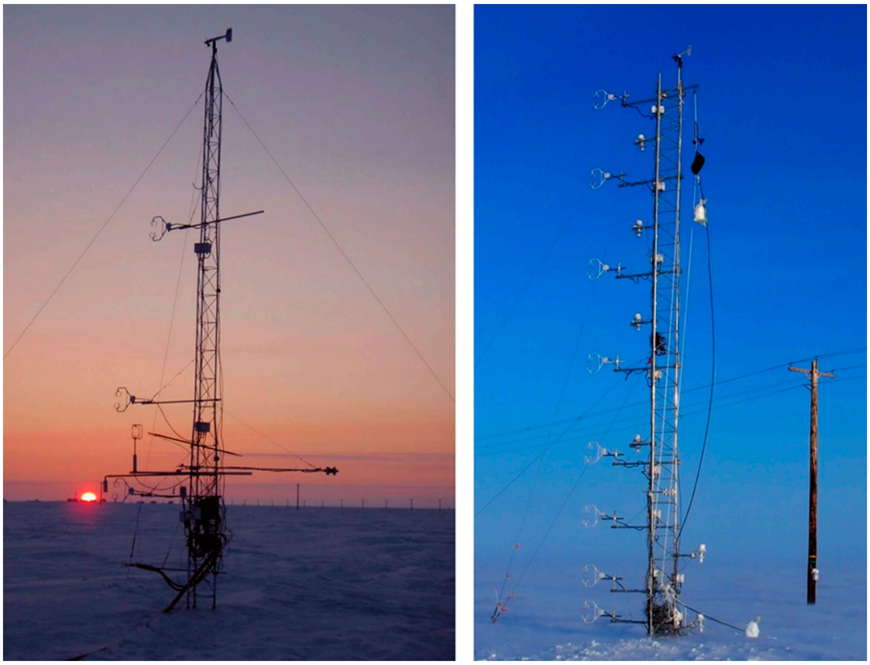

FIG. 1. Photos of the eddy covariance towers (left) B09 (Utqiaġvik OASIS Field Campaign 2009) and (right) B16 (Utqiaġvik PHOXMELT Field Campaign 2016).

intermittently turbulent flow states, displaying variability at multiple time scales, would further exacerbate this challenge. Thus, the final motivating question addressed in section 6 is, How can vertical fluxes across all regimes of stratified turbulence be modeled in a framework commensurate with complexity to existing closure schemes?

This work seeks to elucidate some of the complex physics of intermittently turbulent flows in the strongly stable ASL. Episodes of intermittent turbulence are detected by a combination of two dimensionless parameters that characterize the temporal variability of TKE, and thus measure the degree of departure of the flow from canonical fully developed turbulence (section 3). Flow structures within these regimes are then examined (section 4), and localized turbulent bursts in the weakly turbulent periods are identified and their origins are investigated (section 5). Finally, new closure models for periods in all regimes are proposed and tested (section 6), and conclusions are drawn (section 7). For completeness, an overview of the data and methods is featured first.

2. Data and methodology

a. Field experiments and analyses

Two field studies were undertaken in Utqiaġvik (Barrow), Alaska, to investigate atmospheric turbulence in the ASL. Observations from these two periods B09: OASIS 2009 (Staebler et al. 2009; Perrie et al. 2012; Bottenheim et al. 2013), and B16: Photochemical Halogen and Ozone Exchange: a Meteorological Experiment on Layered Turbulence 2016 (PHOXMELT 2016; Ruiz-Plancarte et al. 2016) are analyzed. Three-dimensional velocity and (sonic virtual) temperature measurements (u, v, w, and $T_s \approx T_v$, where T_v is the true virtual temperature) were recorded. The first campaign "Utqiaġvik OASIS" collected measurements between 6 March and 15 April 2009 at Utqiaġvik (71.323 88°N, 156.662 66°W). Four sonic anemometers were mounted on a 10-m tall tower, 29 m southeast of one of the OASIS instruments trailers (Fig. 1, left). The lowest anemometer (model TR90-AH, Kaijo Denki, Japan) was placed at 0.58 m above the snowpack, had a 5-cm pathlength, and provided data at a frequency of 20 Hz. The other three sonic anemometers (model CSAT3, Campbell Scientific Inc., Logan, Utah) were placed at 1.8, 3.2, and 6.2 m above the snowpack, had 10-cm pathlengths, and provided data at a frequency of 10 Hz. Anemometers were mounted on booms facing the prevailing wind direction (60° from true north). The second dataset from "Utqiaġvik PHOXMELT" includes sonic anemometer measurements at 8 levels (0.5, 1.3, 2.0, 4.0, 5.7, 7.7, 9.7, and 11.6 m) collected at 71.275 19°N, 156.640 00°W, 4 km ESE of Utqiaġvik from 5 March 2016 to 15 May 2017 (Fig. 1, right). The instruments used were all CSAT3 anemometers recoding at a frequency of 10 Hz.

The analyzed data were subjected to linear detrending and despiking: data were separated into running windows of 5 min each, and if the deviation of any instantaneous data point (10- or 20-Hz raw data) from the mean exceeded 6 times the corresponding standard deviation in that window, all four data variables (u, v, w, and T_s) corresponding to that time stamp were removed and replaced with NaNs so they would not affect the statistics. We applied double rotation of wind components based on 15-min time averages, the same period used for Reynolds time averaging throughout. Longer periods up to 30 min were tested, but the results were weakly sensitive to this choice. While longer periods would offer better statistical convergence, they would also result in stronger uncertainties in the statistics with contributions from nonturbulent (submeso and other) motions (Mahrt and Bou-Zeid 2020). Another rationale for choosing 15 min is to prevent multiple shifts among the three turbulence regimes within a single averaging period. Periods characterized by winds blowing from the back of the tower were removed (negative u before coordinate rotation). When blowing snow or riming is present, the transducers of the sonic anemometers trigger error flags and the data quality drops; periods with such flags were omitted.

The local gradients of selected first-, second-, and third-order Reynolds-averaged moments at each level were calculated from the corresponding profiles that were locally fitted to a second-order polynomial. The number of sonic anemometers used in each gradient computation is dynamically chosen such as to mimic centered spatial differencing whenever possible with third-order accuracy (for lowest and highest sonics, second-order one-sided differences had to be used). Only periods characterized by negative heat flux and positive mean temperature gradient (i.e., statically stable) were analyzed. These periods span a wide range of days to avoid biasing for a unique synoptic pattern that might control the flow physics. In addition, days marked by drainage flows due to potential katabatic winds were identified (double peak velocity profiles) and removed from the analyses. A total time span of around 120 h (i.e., 480 × 15-min periods) from both field campaigns met the described criteria and is used in the subsequent analyses.

b. DNS data and analyses

The DNS data are from simulations of a turbulent Ekman flow. Navier–Stokes equations with corresponding boundary conditions are solved for an incompressible fluid under the Boussinesq approximation. A Dirichlet boundary condition is imposed on the buoyancy field at the top and bottom of the domain, while in the horizontal directions, periodic boundary conditions are used. The frictional Reynolds number is defined here as $\mathrm{Re} = GD/\nu = 1000$, where G is the geostrophic wind, $D = \sqrt{2\nu/f}$ the depth of a laminar Ekman layer, ν the kinematic viscosity, and f the Coriolis parameter. All output variables are expressed in nondimensional form where lengths and velocities are normalized by the Rossby radius $\Lambda = G/f$ and G, respectively. The physical setup describes the Ekman layer that develops from the interaction between a flow in geostrophic equilibrium with the no-slip condition $u = \upsilon = 0$ at $z = 0$. Stable stratification is imposed by a negative surface buoyancy $B_{\mathrm{wall}} = B_{\mathrm{ref}}$. The original grid contains 3072 × 6144 × 512 nodes in the streamwise, cross-stream, and vertical directions, while the computational domain has dimensions $1.08 \times 1.08 \times 0.258\ \Lambda^3$. But for the present paper, data are analyzed only over a subset domain that contains five x–y horizontal planes (around $z^+ = 50$ in the log layer) spanning an isotropic 512 × 512 horizontal grid. This covers 1/6 × 1/6 of the whole simulation plane. At each grid point, a time series of 1250 time steps (250 samples taken every fifth time step) of all variables was interrogated. All gradients are computed based on finite differencing using a five-point stencil (fourth-order accuracy). Further details on the setup can be found in Ansorge and Mellado (2014, 2016).

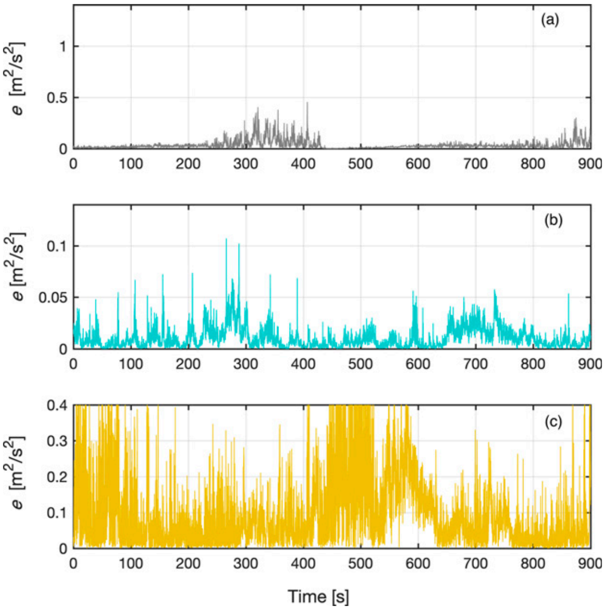

FIG. 2. Illustrations of (top) an intermittent period in regime 1: $[I_{\mathrm{weak}}, \mathrm{CV}_e] = [0.04, 0.85]$; (middle) a transitional period in regime 2: $[I_{\mathrm{weak}}, \mathrm{CV}_e] = [0.06, 0.73]$; and (bottom) a fully turbulent period in regime 3: $[I_{\mathrm{weak}}, \mathrm{CV}_e] = [0.11, 0.69]$. Data are selected from the highest sonic anemometer level at 11.6 m from the B16 field campaign.

3. Intermittency detection and characterization in the observational data

Time series of the instantaneous TKE, $e = (u'^2 + \upsilon'^2 + w'^2)/2$, (Fig. 2), were first inspected visually to identify the regimes of turbulence. Here, the prime of a variable represents a fluctuation from its 15-min time average, which is taken as a surrogate for Reynolds averaging throughout the observational analyses. The TKE of each period was plotted such that the scale of the TKE axis (the y axis) is extended to comprise 25% of the mean kinetic energy of the flow for this period, which then serves as a reference for turbulence-to-mean kinetic energy partitioning (akin to a turbulence intensity). These visual classifications revealed three regimes, which are comparable to the ones identified in the literature surveyed in the introduction. In regime 1, we observed quiescent periods that "look" more laminar-like than turbulent-like, and where turbulent stresses and fluxes play a minor role (periods 0–200 and 430–800 s in Fig. 2a; we refer to them as quasi laminar). In regime 2, turbulence is always present, but with low intensity periods (for instance, 390–580 s in Fig. 2b where the flow is more turbulent-like than laminar-like) intermingled with

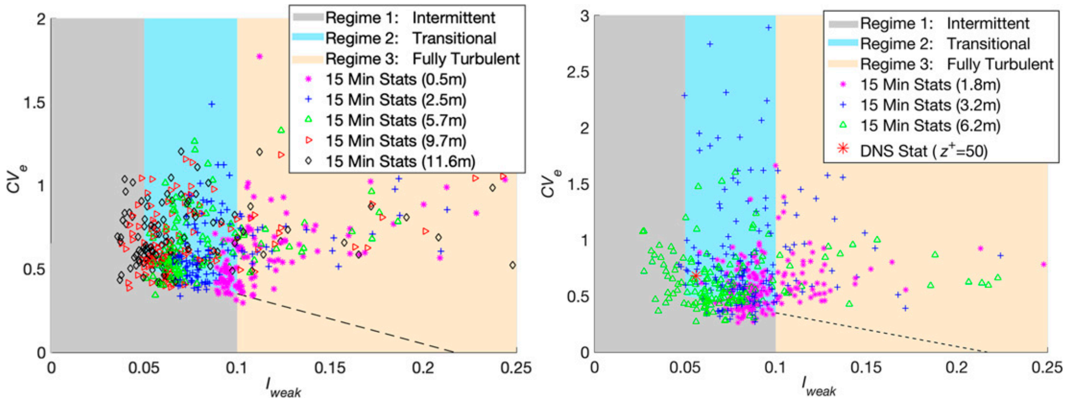

FIG. 3. Scatter of all 15-min periods' statistical stamps in the three regimes based on [I_{weak}, CV_e] parameters at different heights. (left) B16 field campaign, and (right) B09 field campaign and DNS.

periods of moderate intensity with canonical stable ASL turbulence. Regime 3 is the classic fully turbulent flow where turbulence intensity fluctuates but is never "weak" for extended periods (Fig. 2c).

Going back to the quasi-laminar patches of regime 1, the turbulent viscosity averaged over each patch was computed and found to range between 10^{-3} and 10^{-4} $\mathrm{m^2\,s^{-1}}$, which is still larger than the molecular viscosity of air $\approx 10^{-5}$ $\mathrm{m^2\,s^{-1}}$. However, it is orders of magnitude smaller than in the fully turbulent ASL and therefore, during such quasi-laminar episodes, the instantaneous turbulent viscosity might decrease to become on the order of the molecular one. This is the signature of transitional flows (see, e.g., the American Meteorological Society's definition: http://glossary.ametsoc.org/wiki/Transitional_flow) that switches back and forth between turbulent and laminar regions and states. The flow never fully becomes laminar though, leaving weak oscillations that can gradually (see Fig. 2a) grow back into fully developed turbulence. Therefore, the laminarizing patches are intermingled with turbulent periods of low intensity, where turbulence significantly modifies the mean flow. Similar transitions between laminar and turbulent states are also documented by Narasimha and Sreenivasan (1973) for wall bounded flows with a suddenly imposed large favorable pressure gradient, which damps turbulence.

To capture the physical distinctions between these three regimes, we probed a large number of statistical turbulence characteristics (e.g., kurtosis, skewness, anisotropy, bimodality coefficient, variance-to-mean ratio, and turbulence intensity, among many others). We also tested the ability of the k-means clustering algorithm (Lloyd 1982) to reproduce our visual classification by providing it with the TKE time series of our analyzed periods. The latter failed to flag out intermittent periods despite succeeding to discriminate the fully turbulent periods from the other two regimes (it might however have succeeded if other statistics had been provided, not tested here). The statistical indicators empirically found to best flag out or delineate the different regimes, at any measurement level, consist of two nondimensional parameters. The first, I_{weak}, characterizes the weakest turbulence state, while the second, CV_e, describes the range of turbulence variability within the period.

More specifically, the first nondimensional parameter (I_{weak}) is a direct measure of the weakest turbulence states (taken over 10-s patches) within each 15-min window (population of 90 data points). It is quantified as the ratio of the square root of the first quartile Q_1 of the 10-s box-averaged (defined with angle brackets) TKE $\langle e\rangle$, over the bulk velocity $\overline{U}$ of the 15-min time-averaged mean flow (denoted by an overbar). This indicator can be written as

$$I_{\text{weak}} = \frac{\sqrt{Q_{1\langle e\rangle}}}{\overline{U}}. \tag{1}$$

The second nondimensional parameter (CV_e) is the coefficient of variation of $\langle e\rangle$ computed as the ratio of its standard deviation, normalized by its mean, within each period's 15-min record. It is a measure of global variability of turbulence activity within that period:

$$\mathrm{CV}_e = \frac{\sigma_{\langle e\rangle}}{\langle e\rangle}. \tag{2}$$

Investigating each 15-min record at all sonic levels (similar to Fig. 2) enabled us to set empirical thresholds [$I_{\text{weak,crit}}$, $\mathrm{CV}_{e,\text{crit}}$] that can reasonably demarcate the different regimes (Fig. 3). Periods characterized by $I_{\text{weak}} < 0.05$ and $I_{\text{weak}} > 0.10$ correspond to regime 1 "intermittent" and regime 3 "fully turbulent," respectively, regardless of CV_e. Periods with $0.05 < I_{\text{weak,crit}} < 0.10$ may belong to regime 1 or regime 2 "transitional," depending on a threshold of $\mathrm{CV}_{e,\text{crit}}$ ($0.35 < \mathrm{CV}_{e,\text{crit}} < 0.5$), as depicted in Fig. 3. These thresholds are assigned based on the visual categorization of the periods that was done before computation, and without consideration, of the dimensionless parameters.

Periods with [I_{weak}, CV_e] that lie near the regime interfaces feature similar behavior regardless of which side of the interface they lie on. This underscores that there is no clustering of turbulence to well-defined states, but rather a continuous transition (Donda et al. 2015; Deusebio et al. 2015; Van der Linden et al. 2020), and also makes the exact choice of thresholds for $I_{\mathrm{weak,crit}}$, and $\mathrm{CV}_{e,\mathrm{crit}}$ less consequential (these thresholds are thus not exact delimiters, but rather indicative of the values around which the regimes are gradually transitioning; they are not needed in the analyses of sections 4–6). For example, some periods can behave as regime 1 early on, and then switch to regime 2. Specifically, periods near the slanted line demarcating regimes 1 and 2 may mimic the moderately turbulent regime (back and forth between regimes 1 and 2) defined by Sun et al. (2012). This line is slanted because as I_{weak} (weakest turbulence state) intensifies and approaches the critical value $I_{\mathrm{weak,trans}} = 0.10$ (the boundary beyond which the fully turbulent regime 3 prevails), smaller CV_e (less variability) is sufficient to define the period as transitional rather than intermittent (lower variability is sufficient for continued turbulence activity if the calmest periods are more energetic).

While I_{weak} and CV_e are height dependent and in fact encode height information (the higher the elevation the weaker turbulence in general becomes) as revealed in Fig. 3, the present analyses suggest that the same values of their thresholds [$I_{\mathrm{weak,crit}}$, $\mathrm{CV}_{e,\mathrm{crit}}$] can be used for all sonic levels (to concur with our visual classification), making this nondimensional classification height independent (at least in the present datasets). The exact thresholds, especially for the $I_{\mathrm{weak,trans}}$, could however be site dependent since the onset of continuous turbulence might be aided by topography, heterogeneity, and surface roughness. Mapping the regimes defined in Fig. 3 to the regimes identified by Sun et al. (2012) at all levels reveals that regime 1 in our classification corresponds to regime 1 "weakly turbulent regime" in Sun et al.'s definition, whereas their regime 2 "strongly turbulent regime" maps to our regime 3. Using dimensional metrics based on mean wind speed, such as those used in HOST, previous analyses found a decrease of the threshold mean wind with increasing roughness (Mahrt et al. 2013). The net radiation and surface thermal characteristics, suggested by Van de Wiel et al. (2012), might also affect the specified HOST mean wind threshold. Mahrt et al. (2015) further identified the effect of the vertical potential temperature difference, between the level of the observation and the surface, on the mean threshold wind speed and confirmed that the stratification will have an impact on a dimensional wind shear metric. Other factors such as site-dependent nonstationarity, directional wind shear (Ghannam and Bou-Zeid 2020), or submeso motions may introduce a site dependency for the relation between the strength of turbulence and the mean flow in stable conditions as well (Acevedo et al. 2013).

The two newly proposed dimensionless parameters are devised to detect intermittency and classify the turbulence regimes, rather than to predict them from synoptic and mesoscale conditions and surface characteristics. Nevertheless, confirming (or disproving) the universality or near-universality of the thresholds $I_{\mathrm{weak,crit}}$ and $\mathrm{CV}_{e,\mathrm{crit}}(I_{\mathrm{weak}})$ under a broader range of synoptic and surface conditions requires further support at other observational sites: the fact that the proposed parameters are dimensionless is a necessary but not a sufficient condition to confirm the wider applicability of this classification based solely on these two numbers. The need for a second discriminator in our method in the vicinity of regime transitions further supports the findings of Van Hooijdonk et al. (2018). It is also comparable to the classification of Deusebio et al. (2015), who explored the boundary between fully developed turbulence and intermittent flow in the Reynolds–Richardson plane (with wall enstrophy as the metric to identify laminar and turbulent patches).

Another feature to observe in Fig. 3 is that the distance from the surface modulates the scatter of the data in the [I_{weak}, CV_e] phase space. Fully turbulent periods (characterized by mild stability, i.e., by weakly positive flux Richardson numbers) dominate at the first level (Fig. 3), whereas intermittent periods become more likely, and the data points shift to the left, with increasing height. This is not surprising as mechanical production of TKE scales with z^{-1}. It would be of interest to couple the nondimensional classification here to the approaches introduced by Vercauteren and Klein (2015), who applied a statistical clustering methodology based on a bounded variation finite element method (FEM-BV) to characterize intermittent bursts of turbulence and their interaction with submeso motions in the stable ASL. Their clustering method separates periods with different influence of the nonturbulent motions on the vertical velocity fluctuations, and this might allow us to understand which interactions dominate at different heights and in different regimes.

4. Flow structures within the different regimes

To investigate the topological differences of the flow structures in these regimes, a pseudocolor plot movie (see movies through the link provided in appendix A) from the B16 tower data was created at all levels, depicting the vertical velocity perturbations and the kinematic heat flux. We identified 3 periods where the sonic anemometer time series at most heights fell within one regime (with the aid of Fig. 3). To construct these movies, we produce x–z vertical slices by invoking Taylor's frozen turbulence hypothesis at each height (with its own mean velocity) and locating the tower in the middle of the resulting domain (appendix A, data are normalized by the standard deviations of vertical velocity and temperature over the 15-min period). While the inaccuracy of Taylor's hypothesis creates some distortion in the coherent structures that one should be mindful of, well-defined flow structures can be detected in each regime as depicted in the snapshots of Fig. 4.

In the intermittent period, the vertical fluctuations always reveal consecutive strong dipoles, i.e., positive–negative pairs, which could be associated with slow near surface waves or hairpin-like vortices. These structures are fully confined within the first 6 m, and the flow above that level is quiescent, with no significant vertical perturbations. These repeated changes in the sign of vertical velocity perturbations in the lower part of the ASL have the potential of interacting with, or even changing, the local stability (at a given height). The number, strength, and orientation of these dipoles, along with local stability, will determine the rate at which these perturbations grow or decay, or if they overturn and enhance mixing. These

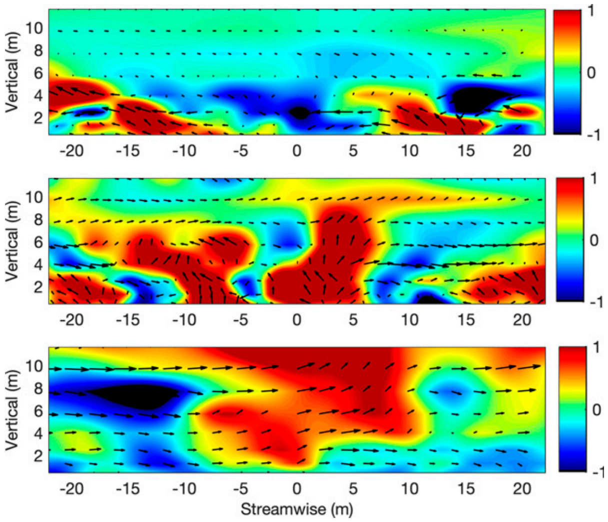

FIG. 4. Pseudocolor plots of the normalized vertical turbulent velocity component in x–z vertical planes for (top) intermittent, (middle) transitional, and (bottom) turbulent periods, with the (u', w') velocity vectors overlaid (B16 data). Mean velocity for each 15-min period is from left to right.

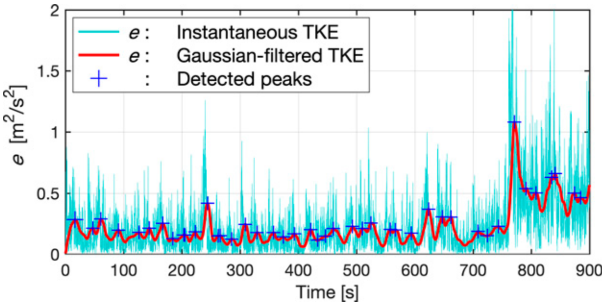

FIG. 5. Peaks detection procedure: instantaneous TKE (solid thin cyan), Gaussian-filtered TKE (solid thick red), TKE bursts' peaks (blue crosses). A random period was chosen for illustration from the sonic anemometer deployed at 0.5 m above the surface of the B16 field campaign.

findings agree with those of Deusebio et al. (2015), who concluded that in the high Reynolds number and high Richardson number intermittent regimes turbulence is confined vertically, with complex dynamics arising from interacting turbulent layers. In the transitional periods, similar dipoles are observed, but they establish themselves across the whole height of the tower, with enhanced heat transfer (see movies in appendix A). For the fully turbulent period, we observe larger structures spanning the whole domain depth. Such dynamics favor the fast and continuous overturning of the flow, preventing stratification. One can also observe that shearing is minimal during these periods where the flow is advected by nearly the same mean wind speed at all levels, except very close to the surface.

Some remarkable features that we should highlight in the movies are the fast waves propagating during the intermittent and transitional periods at higher levels, and that do not seem to interact strongly with the turbulence beneath.

5. The origin of the turbulent bursts

With the [I_{weak}, CV_e] framework for classifying regimes established, the origin of each burst within each of those periods is now analyzed. The aim is to understand their genesis, and whether they are produced locally or advected onto the sensor location.

a. Peaks detection algorithm

Since peak detection applied to the instantaneous observational data will result in multiple peaks within a burst's lifetime due to the strong fluctuations of instantaneous TKE, we apply a low-pass Gaussian filter to the 10-Hz TKE time series. The time scale of the filter, τ_f, is determined dynamically such that the retained and resolved turbulence carries at least 80% of the total (unfiltered) TKE in each 15-min period. This resulted in a $\tau_f \leq 5$ s for all periods and all heights, and in a dynamic value of τ_f that decreased at higher elevations. Peaks are then detected in this filtered time series using a built-in MATLAB function "findpeaks," to which we provide the minimum peak width (MINW = 1 s) and offset/distance between peaks (MPD = 1 s). A sample output of this peak detection is illustrated in Fig. 5. We should underline that the filtered signal is only used for peak and burst detection. The subsequent analyses over a burst revert to using the raw full signal.

b. The genesis of the bursts

The origin of the bursts is investigated by quantifying/estimating all the terms in the burst-averaged TKE budget equation (Stull 2008). This analysis is conducted only for the periods belonging to regimes 1 and 2, where the TKE budget is analyzed dynamically across all bursts. Specifically, we take the averages during the period of turbulence buildup, i.e., from the start of the burst rise till burst peak, in all detected events. These averages over burst-rise lifetime are denoted with an overtilde, yielding

$$\frac{\partial \widetilde{e}}{\partial t} + \widetilde{U}\frac{\partial \widetilde{e}}{\partial x} = \frac{g}{\widetilde{T_v}}\widetilde{(w'T_v')} - \widetilde{u'w'}\frac{\partial \widetilde{U}}{\partial z} - \left[\frac{\partial \widetilde{u'e}}{\partial x} + \frac{\partial \widetilde{v'e}}{\partial y} + \frac{\partial \widetilde{w'e}}{\partial z}\right] - \frac{1}{\overline{\rho}}\left[\frac{\partial \widetilde{u'p'}}{\partial x} + \frac{\partial \widetilde{v'p'}}{\partial y} + \frac{\partial \widetilde{w'p'}}{\partial z}\right] - \varepsilon. \tag{3}$$

The viscous transport and turbulence-mean stress gradient interaction terms are ignored because they are much smaller in magnitude than the other terms. This is later confirmed in the analysis of DNS data. The pressure transport term could not be calculated, as field pressure measurements at high frequencies are not available. While it is usually found to be a small contributor to the budget of the mean TKE in the surface layer of neutral and mildly stable flows (Shah and Bou-Zeid 2019), an objection can be raised here because a filtered instantaneous, not mean budget, is being considered and the pressure transport term may be locally large in magnitude. This objection will indeed prove valid, as we will discuss in the section analyzing DNS data. The streamwise (x) and cross-stream (y) gradients do not drop out despite the fact that the surface is presumed homogeneous because the aforementioned equation is a filtered instantaneous budget (except for the turbulence-mean stress gradient interaction because it involves mean stress gradients that are zero in x and y due to homogeneity, and small in z, as the DNS results later confirm). Terms involving vertical gradients are computed based on fitting a second-order polynomial as explained earlier.

The tendency, buoyant production/destruction, mechanical shear production, and vertical turbulent transport are computed directly from measurements. The x-horizontal turbulent transport term can be estimated by invoking Taylor's frozen field hypothesis $\widetilde{\partial x} \approx -\widetilde{U}\widetilde{\partial t}$:

$$\frac{\widetilde{\partial u'e}}{\widetilde{\partial x}} \approx -\frac{1}{\widetilde{U}}\frac{\widetilde{\partial u'e}}{\widetilde{\partial t}}. \qquad (4)$$

While the y-horizonal turbulent transport term could not be computed since the cross-stream mean velocity is zero and we do not have a lateral array of sensors, it is expected to be a minor contributor to the budget since we rotate the time series into the mean wind direction. The rate of TKE dissipation is estimated using the second-order structure function ($D_{u,u}$) evaluated with an appropriate dynamic value of the time lag in the inertial subrange, $\varepsilon = 0.3634r^{-1}[D_{u,u}(r)]^{3/2}$ (Chamecki et al. 2017), where r is also found by invoking Taylor's frozen field hypothesis. For each burst rise record, $r^{-1}[D_{u,u}(r)]^{3/2}$ is plotted versus the time lag, and a proper lag (inertial subrange time scale) is selected when $r^{-1}[D_{u,u}(r)]^{3/2} \approx$ const, forming a plateau if possible (Pope 2000). The mean advection of TKE cannot be directly calculated or estimated and hence it is taken as the residual of the budget, which implies that the unquantified pressure transport and cross-stream turbulent advection, and any errors in the computations of the other terms, are also embedded in this estimate. But we will interpret it as a mean advection since we expect this to be the dominant term in the residual (later confirmed by DNS).

The analysis focuses on the identified bursts during intermittent/transitional periods (corresponding to all bursts in regimes' 1 and 2 periods in Fig. 3) where a one-to-one correspondence is observed in Fig. 6 between the positive tendencies and the dominant TKE term in Eq. (3). A magnitude intercomparison analysis among the TKE terms reveals the one most responsible for the rise in TKE during each turbulent burst. Figure 6 is a summary of these dominant TKE budget terms explaining the positive tendencies. The plotted bin-averaged data in Figs. 6–9 and Fig. B1 are computed over half decades (if and only if more than 20 points exist within a bin) (Muschinski et al. 2004). At the first level, the top row of Fig. 6 indicates that local mechanical shear production explains 53% of the total bursts (Fig. 6b), streamwise TKE advection by the mean flow contributes around 40% (Fig. 6c), and 7% are attributed mainly to vertical turbulent transport (Fig. 6a). Vertical and horizontal turbulent transport are plotted separately to assess the contribution of each, but if the two were combined, their sum would better track the one-to-one line matching the tendency (not shown). The results suggest, given the dominance of mean over turbulent advection, that even the advected turbulence bursts are most likely associated with height-local, but upstream shear produced turbulence.

Vertical turbulent transport becomes more substantial (explaining 33% of the burst rises) at the higher sonic anemometer level, as depicted in the bottom row of Fig. 6d, at the expense of the mechanical shear production (Fig. 6e). The latter decreases to 9%, while the streamwise TKE advection by the mean flow increases to 58% (Fig. 6f). This crucial increase in the contributions of transport mechanisms, either by upward vertical turbulent transport (since we confirmed that $w' > 0$ for most of the bursting events at higher elevations) or by streamwise mean advection, indicates that the source of turbulence is mostly at the surface (the shear generation that dominates for the lower levels). Some events of local buoyant production were also noticed; these are likely to be air parcels that were pushed too far from their equilibrium state and are being accelerated by buoyancy on their return to their equilibrium level, converting turbulent energy from potential to kinetic (Zilitinkevich and Esau 2007).

If one considers regime 3 solely (the fully turbulent periods, see Fig. B1 in appendix B), streamwise TKE transport by the turbulence field becomes notable, and stronger sometimes than vertical turbulent transport at the lowest level. Generally, the turbulent transport mechanisms become almost as important as mean flow advection of TKE (unlike the results in regimes 1 and 2 that show a dominance of the latter); however, mechanical shear contribution is roughly invariant in comparison with regimes 1 and 2. Similar statistical findings were also established for the B09 data field campaign (not shown).

As stated in the introduction, locally intermittent turbulence in observations is usually attributed to a variety of external disturbance mechanisms and mesoscale phenomena (Sun et al. 2002, 2004; Banta et al. 2007; Cuxart et al. 2007). The present observational results do not negate this possibility since one cannot be certain of the origin of the bursts that are advected horizontally past the sensor either by the mean flow or by the perturbations. However, the decrease in the intensity of turbulence and the increase in the role of upward vertical transport with height, coupled with the preponderance of locally shear generated bursts at lower levels, suggest that mechanical shear production is itself sufficient for the maintenance of intermittent turbulence under higher stability. Since tower measurements are conducted at a fixed point, bursts that are shown to be advected past the sensors could also have been generated by mechanical shear locally upstream of the tower. Therefore, the present results confirm that intermittency is a phenomenon inherent to the stable ASL and does not necessarily need any external triggering mechanisms in agreement with other studies (Ansorge and Mellado 2014,

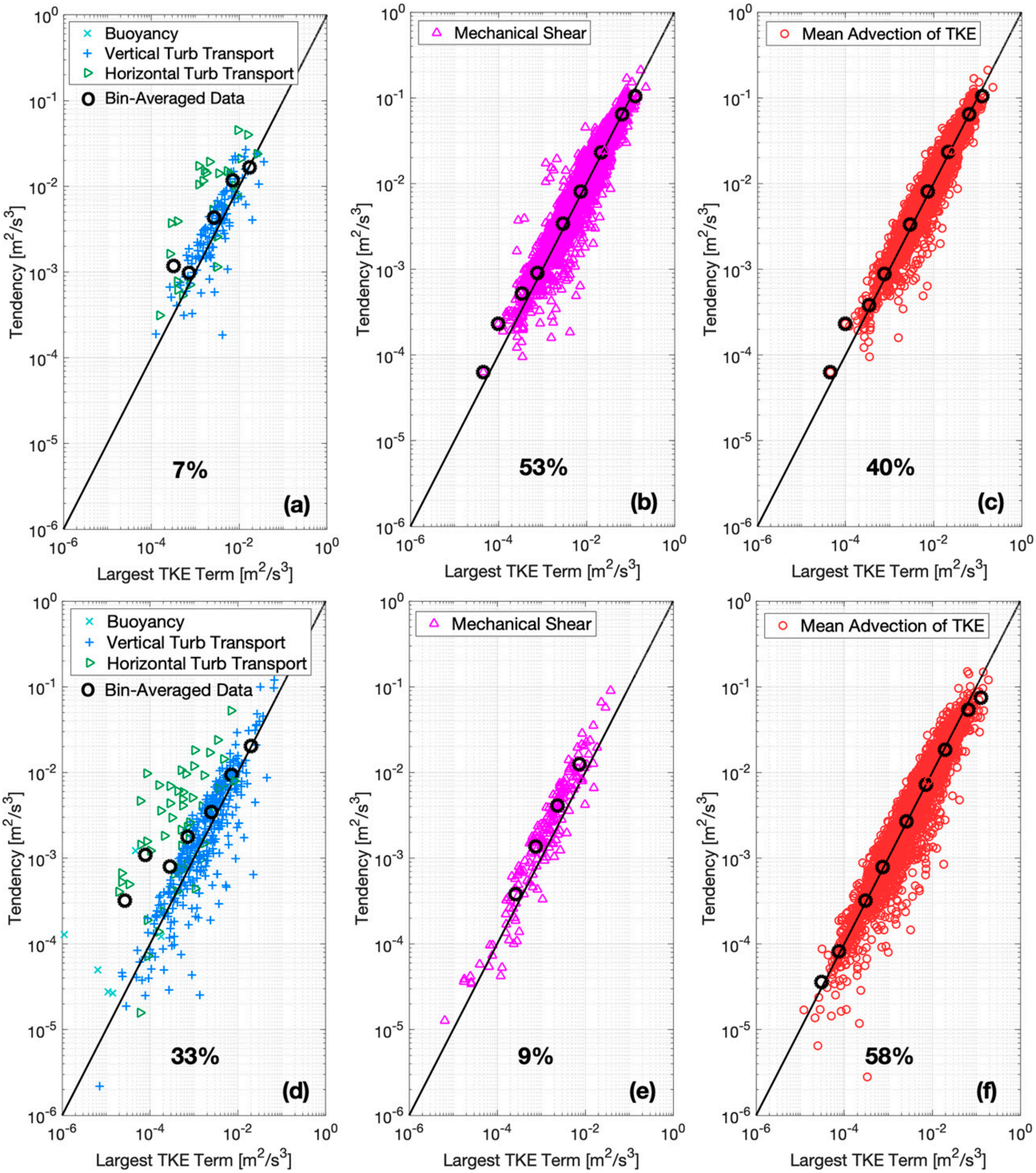

FIG. 6. Bursts' rise origins in regimes 1 and 2: (a)–(c) first level (0.5 m) and (d)–(f) eighth level (11.6 m). The solid black line is the one-to-one line for reference. Data are from the B16 field campaign. Bin-averaged data are applied over half decades (if and only if more than 20 points exist within a bin).

2016). This will be confirmed by the DNS results presented later. Furthermore, our findings support the hypothesized one-dimensional model for intermittent turbulence in the stable ASL proposed by Costa et al. (2011), where bursting events are shown to be generated by shear production near the surface, and their upward propagation is mainly driven by the turbulent transport term.

External triggers, such as LLJs, cannot be fully examined in the available data because of the tower's height restriction of 11.6 m or absence of needed instruments (e.g., fast pressure

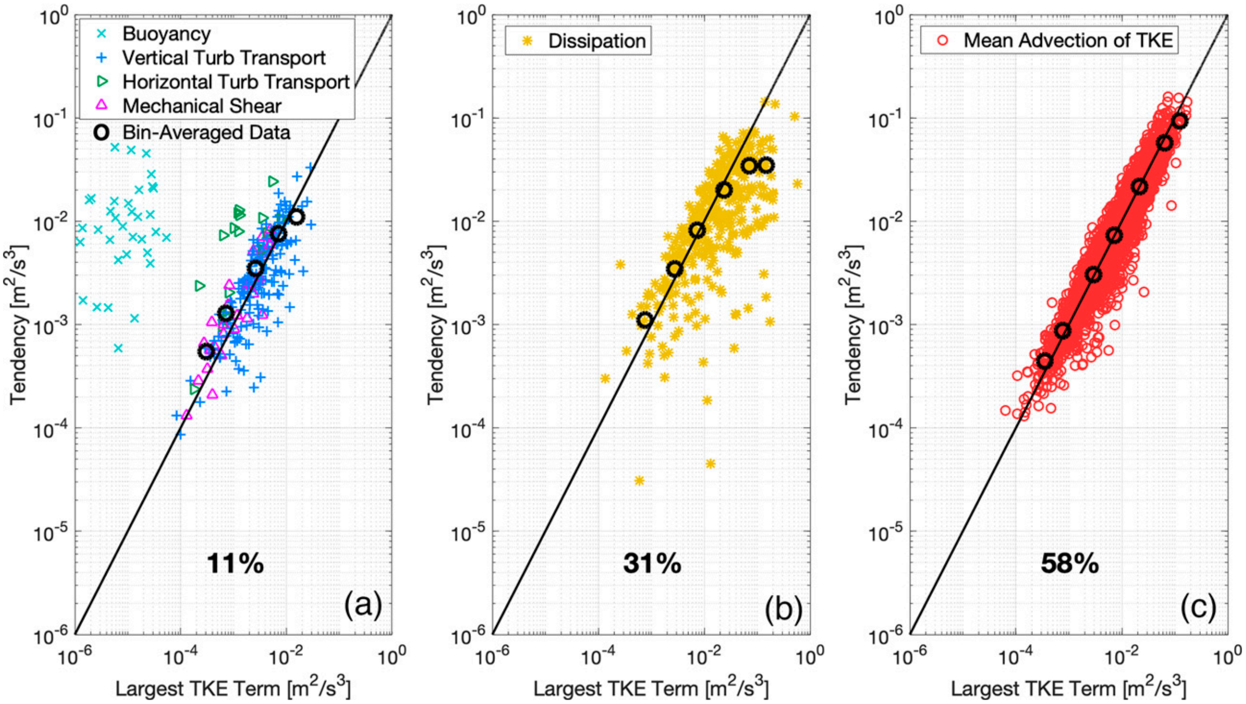

FIG. 7. Bursts' decay physics in regimes 1 and 2: one-to-one reference (solid black line). Data from the first level (0.5 m) at B16. Bin-averaged data are applied over half decades (if and only if more than 20 points exist within a bin).

sensors). But their effect would be to alter the percentages in the analyses above. The probability of LLJ playing a key role, however, is not supported by these measurements for our sites since downward TKE transport is uncommon. This is consistent with the fact that the weak polar diurnal cycle is expected to lead to weaker inertial oscillations and weaker LLJs (though there are other mechanisms to trigger oscillations and LLJs; e.g., Du and Rotunno 2014; Momen and Bou-Zeid 2016). Therefore, the physics governing intermittency at these high latitudes sites seem to be mostly triggered locally by internal turbulence mechanisms and bottom-up turbulent events, unlike some previously investigated sites at midlatitudes (e.g., CASES-1999).

c. The decay of the bursts

As suggested by Ansorge and Mellado (2014, 2016), surface layer dynamics also control the relaminarization process. Hence, the TKE budget equation is revisited again dynamically across all bursts, but now considering the decay of turbulence, i.e., from burst peak till burst decay. Figure 7 summarizes the dominant TKE terms describing the negative tendencies (y axis and x axis multiplied by -1 to plot on a log–log scale) observed during the falling limbs. We find that relaminarization is primarily controlled by dissipation and streamwise mean advection of TKE, i.e., bursts advected onto the tower are advected away. Turbulent transports, as well as global backscatter (negative shear production), explain the decay in some events as well. Only few periods where buoyancy partially (points significantly away from the one-to-one line) explains the decay are observed, hinting at the indirect role of buoyancy as a TKE sink in such flows as illustrated using DNS by Shah and Bou-Zeid (2019). If one considers regime 3 solely (not shown), the turbulent transport mechanisms become more effective and important at the expense of dissipation.

d. TKE bursts investigation using DNS data

The origin of turbulent TKE bursts was also investigated using DNS data. First, we computed all terms (without simplifications) in the instantaneous TKE budget equation:

$$\frac{\partial e}{\partial t} + \overline{U}_j \frac{\partial e}{\partial x_j} = \frac{g}{\overline{T}_v}(w' T_v') - u_i' u_j' \frac{\partial \overline{U}_i}{\partial x_j} - \frac{\partial u_j' e}{\partial x_j} - \frac{1}{\overline{\rho}} \frac{\partial u_i' p'}{\partial x_i} + \nu u_i' \frac{\partial^2 u_i'}{\partial x_j^2} + u_i' \frac{\partial \left(\overline{u_i' u_j'}\right)}{\partial x_j}. \quad (5)$$

The overbar in Eq. (5) denotes averages over x–y horizontal planes (interpreted as Reynolds averages), and statistical homogeneity holds in the x "streamwise" and y "cross-stream" directions. Coriolis terms are identically zero in kinetic energy equations since it is a conservative pseudoforce that can only redistribute energy between the three components (Stull 2008; Momen and Bou-Zeid 2016). Note that the last term is the turbulence-mean stress gradient interaction that is identically zero for the mean TKE budget, but it needs to be retained for its instantaneous counterpart; it is however found to be negligible for the case investigated here confirming our assumption for the observational data analysis.

To mimic as closely as possible the observational data analysis over bursts, we average the instantaneous DNS budget terms

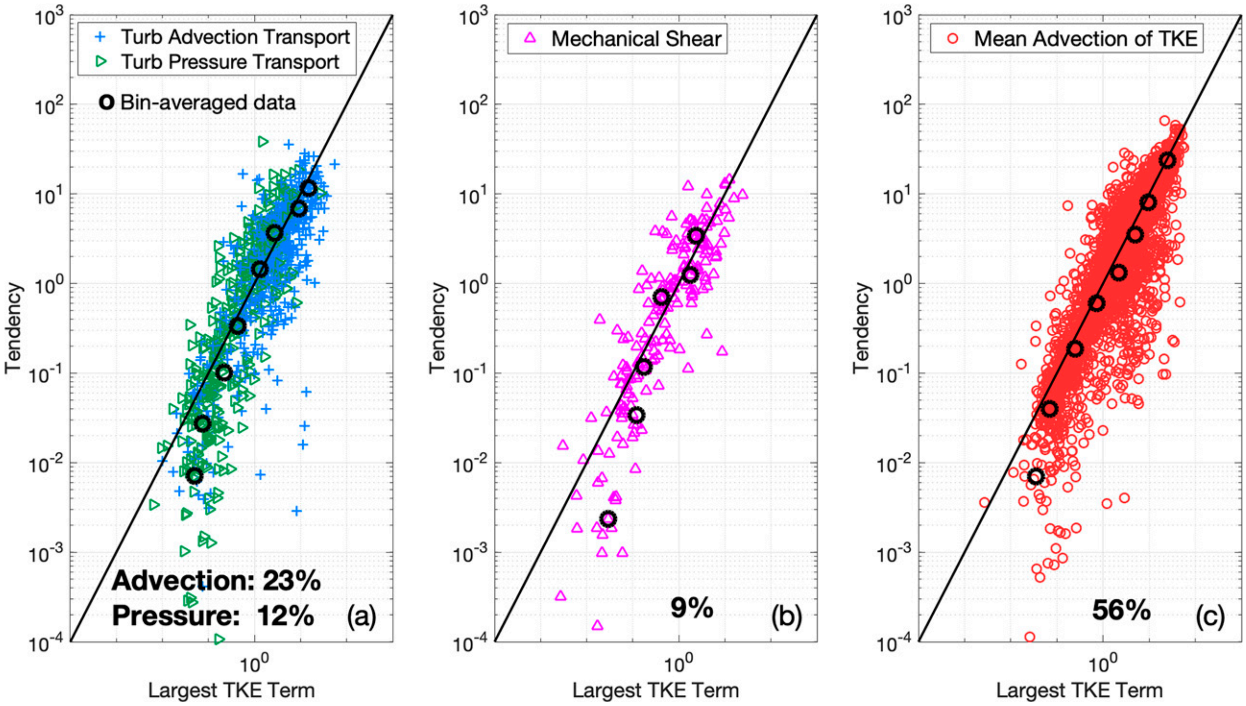

FIG. 8. Bursts' rise origins from the DNS instantaneous TKE at $z^+ = 50$. One-to-one line is shown for reference (solid black line). Bin-averaged data are applied over half decades (if and only if more than 20 points exist within a bin).

over events with at least three consecutive points of positive tendencies depicting a burst rise. This mirrors the peak detection that allowed us to delineate bursts in the observational data, but was found more suitable for the DNS analysis since the data records are short with fewer peaks. The analyses are applied to time series at multiple randomly selected spatial points.

In the present DNS analyses, all terms can be quantified without any modeling involved, including the pressure transport and mean advection, and the numerics are sixth-order accurate in the interior of the simulation domain. Therefore, Taylor's frozen turbulence hypothesis is not needed because all spatial gradients could be computed. The averaged nondimensional statistical metrics for these DNS time series are $[I_{\mathrm{weak}} = 0.056, \mathrm{CV}_e = 0.68]$. These metrics place the DNS data near the interface between regimes 1 and 2, so these periods have intermittent and transitional features (weakly turbulent mode, as shown in Fig. 3, right panel). Figure 8 is a summary of the dominant TKE terms explaining the bursts observed. The percentages of dominant terms are roughly 56% for the mean advection of instantaneous TKE and 9% for mechanical shear, closely aligned with the higher-level statistics in the field data. While this may seem counterintuitive since the DNS height of $z^+ = 50$ is much smaller than the field observational elevation in these inner coordinates, one should note that the whole DNS domain for a statically neutral simulation would have a height of $z^+ \approx 870$ for our setup. Thus, if the inertial or log layer is 10% of that (extending to $z^+ \approx 87$), then $z^+ = 50$ is relatively high in the ASL, and more comparable to our higher field level. Turbulent pressure transport (which was not computable and thus neglected in the experimental data analysis) accounted for 12% of the rise in TKE, and turbulent transport mainly in the vertical accounted 23% (again comparable to the higher-level field data). Mean advection is responsible for positive tendencies that may be one order of magnitude larger than the contribution of mechanical shear, as shown in Fig. 8. That is, strong bursts cannot be generated locally; they would have to be generated upstream and evolve and strengthen before reaching a sampling location.

Overall, the DNS results concur favorably with the field data (particularly the higher level), illustrating that commonly observed difficulties in estimation of higher-order terms from field data do not affect the broad conclusions we draw. The main difference in the results between DNS and the upper level of the field data is the detectable role of turbulent pressure transport in the simulations. Most likely, this contribution was comparable but not computable in the field data. However, given the sensitivity of the results to height, and the fact that the observational and DNS heights do not match exactly (despite being in the ASL), the exact quantitative differences should be interpreted with caution. It is also possible that pressure transport is more prominent in the DNS data due to the lower Reynolds number, but we can only hypothesize this in the present analysis given the available field data.

6. Flux modeling

a. *Transport efficiency during bursting*

The above analysis shows—in accordance with previous work (Deusebio et al. 2015; Ansorge and Mellado 2016)—that a physics based model for turbulent mixing in such intermittently turbulent flows cannot rely on bulk statistics but may require conditional analysis (Antonia 1981). The burst detection approach establishes a physically meaningful partitioning of the flow periods, such that a turbulent transport efficiency for bursting periods can be estimated. A relative turbulent transport efficiency (η_{tur}^{Φ}) for any instantaneous turbulent flux quantity Φ (e.g., heat or momentum) can be estimated as the flux averaged over bursts normalized by the flux over the whole 15-min period, that is $\eta_{\text{tur}}^{\Phi} = \widehat{\Phi}/\overline{\Phi}$, where the angled hat denotes averaging over all bursting subperiods $\widehat{\Delta t_{tur}}$ within a 15-min period. The conditionally averaged flux during bursts is computed as

$$\widehat{\Phi} = \sum_{p} B\Phi_{p} \Big/ \sum_{p} B, \tag{6}$$

where the summation is over all instantaneous points p, and the conditional indicator is $B = 1$ if $\{p \in \text{bursting period}\}$ and $B = 0$ otherwise (Antonia 1981).

When computed, these relative efficiencies have the same order of magnitude across all regimes. This efficiency is also found to be about 4 times larger than the transport efficiencies during laminarizing subperiods (computed in the same way but with the conditional indicator $L = 0$ if $\{p \in \text{bursting period}\}$ and $L = 1$ otherwise; that is $L = !B$, where ! is the logical NOT operator). This further corroborates the main findings of Ansorge and Mellado (2016), who concluded that the properties and scaling of fully turbulent patches under strongly stable intermittent regimes are comparable to those under mildly stable regimes, but it is rather the size/frequency of the turbulent fraction that changes.

b. *Flux modeling and mixing length scale identification*

With this distinction between transport efficiency during turbulent and laminarizing subperiods, we turn our attention to the modeling of the fluxes averaged over 15-min periods in the three regimes (with a focus on the intermittent and transitional ones). In this part, we formulate the model using the conventional atmospheric sciences coordinate system used in the previous sections to analyze sonic anemometer data: x and u are in the streamwise direction along the wind, y and v in the cross-stream direction, and z and w in the vertical direction, oriented opposite to gravity. In appendix C, we provide the closure formulations in a Galilean-invariant form in generalized coordinates.

Tracking the kinematic fluxes (of momentum and heat) of all detected bursts, averaged over the lifetime of the burst, suggests a strong correlation with vertical velocity variance $\overline{w'^2} = \sigma_w^2$ (not shown). In addition, the relatively high value of $\eta_{\text{tur}}^{\Phi} \approx 1.28$ confirms that the bursts are the major contributor to the fluxes for regimes 1 and 2; the less turbulent or laminar events have a smaller efficiency $\eta_{\text{lam}}^{\Phi} \approx 0.34$. Therefore, bursts dominate vertical transport and they enhance flux efficiency, on average, by a factor of 3.76 (=1.28/0.34). In developing a closure model, the commonly used eddy diffusion representation for fluxes is first examined using

$$\overline{u'w'} = -K_m \frac{\partial \overline{U}}{\partial z}, \tag{7a}$$

$$\overline{w'T_v'} = -K_h \frac{\partial \overline{T}_v}{\partial z}, \tag{7b}$$

where the eddy diffusivities are defined using the standard deviation of the vertical velocity:

$$K_m = \sigma_w L_m, \tag{8a}$$

$$K_h = \sigma_w L_h. \tag{8b}$$

This representation is in keeping with Lagrangian structure function analysis, where $K_m = 2\sigma_w^2 \tau_L$ (Taylor 1922) and τ_L is related to a Lagrangian time scale. Another advantage of this representation is that it ensures a positive definite eddy diffusivity, while turbulent diffusivity representations based on Prandtl's mixing length hypothesis (i.e., $L_m^2 \partial \overline{U}/\partial z$) do not, a result known all too well in canopy flows that experience a secondary maximum (Shaw 1977).

Since turbulent fluxes are dominated by the larger eddies, the mixing length scales L_m and L_h should capture these integral scales. Therefore, the mixing length scales are defined as hyperbolic averages of two scales that are competing to limit the size of the largest eddies, so that the smaller limiting length scale has a stronger impact on the outcome [Eq. (9c) below]. For momentum, after empirical evaluation of a wide range of plausible length scales that were used in previous literature, L_{m1} [w-variance based shear length scale, Eq. (9a)] and L_{m2} [the classic shear length scale, Eq. (9b); Stull 2008] are found to yield the best flux results:

$$L_{m1} = (1 - \alpha_m)\sigma_w \left(\frac{\partial \overline{U}}{\partial z}\right)^{-1}, \tag{9a}$$

$$L_{m2} = \alpha_m \overline{U} \left(\frac{\partial \overline{U}}{\partial z}\right)^{-1}, \tag{9b}$$

$$L_m = \left(\frac{1}{L_{m1}} + \frac{1}{L_{m2}}\right)^{-1}. \tag{9c}$$

All variables in Eqs. (9a) and (9b) are time averaged over the 15-min duration of each period, and thus no distinct averages over the quasi-laminar phase and the fully turbulent phase are invoked. The α_m is an empirical constant that reflects the fraction of the time each of the two length scales dominates, tuned empirically to $\alpha_m = 0.35$ to provide the best match to field data for B09, and kept the same for B16 for blind testing. This weighing scheme is analogous to what was derived for canopy flows where momentum transport was dominated by Kelvin–Helmholtz instabilities and attached eddies (Poggi et al. 2004). It is also consistent with the observations of Sun et al. (2012), who found that the turbulence strength in the weakly turbulent regime is correlated with the local shear $\partial \overline{U}/\partial z$, which is the inverse of the turbulent time scale of both length scales proposed above. This may suggest that locally generated weak eddies do not interact strongly with the Earth surface, a regime often called the "decoupled boundary layer" (Acevedo and Fitzjarrald 2003; Mahrt and Vickers 2006). We should also point out that $\overline{U}$ in Eq. (9b) represents the momentum deficit at height z relative to the surface [i.e., the bulk shear $\Delta\overline{U} = \overline{U}(z) - \overline{U}(z_0) = \overline{U}(z)$].

We further observe that for periods in the weakly turbulent mode, i.e., regime 1, L_{m1} is dominant over (smaller than) L_{m2}, which implies that momentum fluxes in Eq. (7a) recover a variance model (no longer an eddy diffusion model) of the form

$$\overline{u'w'} = -(1 - \alpha_m)\sigma_w^2. \tag{10a}$$

This model indicates that local fluxes are not linked to the surface and to bulk shear, agreeing with the findings of Williams et al. (2017), who observed in wind tunnel measurements of an SBL that strong stability is associated with a decoupling of the turbulence state from wall stress. On the other hand, turbulence generation in the transitional turbulent mode (i.e., regime 2) is mainly attributed to the bulk shear $\overline{U}/z$. Therefore, for moderate turbulence and closer to the ground, both local and bulk shear are important as pointed out by Sun et al. (2012), and the momentum fluxes in Eq. (7a) recover a bulk model that depends on the mean flow velocity $\overline{U}$:

$$\overline{u'w'} = -\alpha_m \sigma_w \overline{U}. \tag{10b}$$

Both flux expressions are properly defined even in the limit $\partial\overline{U}/\partial z \to 0$, where the mixing length scales $\to \infty$. Therefore, the flux expressions are used directly in the calculations (without the need to compute the length scales explicitly).

Similarly for the mixing length scales for heat, we found that L_h is best expressed as the hyperbolic average of L_{h1} [Eq. (11a)], also known as the Ellison length scale (Ellison 1957), and L_{h2}, the buoyancy length scale given in Eq. (11b) (Stull 1973; Zeman and Tennekes 1977). Noting that L_{h1} can be reformulated in terms of the Brunt–Väisälä frequency $N_{\mathrm{BV}} = \left(g\overline{T_v}^{-1}\partial\overline{T}_v/\partial z\right)^{1/2}$ and the turbulent potential energy $2\mathrm{TPE} = g\overline{T_v}^{-1}\left(\partial\overline{T}_v/\partial z\right)^{-1}\sigma_{T_v}^2 > 0$ (Zilitinkevich et al. 2013), these length scales are given by

$$L_{h1} = \alpha_h \sigma_{T_v}\left(\frac{\partial\overline{T}_v}{\partial z}\right)^{-1} = \alpha_h \frac{\sqrt{2\mathrm{TPE}}}{N_{\mathrm{BV}}}, \tag{11a}$$

$$L_{h2} = (1 - \alpha_h)\frac{\sigma_w}{N_{\mathrm{BV}}}, \tag{11b}$$

$$L_h = \left(\frac{1}{L_{h1}} + \frac{1}{L_{h2}}\right)^{-1}. \tag{11c}$$

The turbulent time scale in both expressions is the inverse of the Brunt–Väisälä frequency. The L_{h1} formulation agrees with the findings from Sun et al. (2012), who showed the kinematic heat flux normalized by the friction velocity, represented by $\theta_* = \overline{w'T_v'}/u_*$, is linearly correlated with temperature fluctuations σ_{T_v} at each level in the weakly turbulent mode, as turbulence is building up (regime 1). As for L_{h2}, it physically encodes the buoyant force experienced by a parcel of air displaced from its equilibrium at a given stratification strength $\partial\overline{T}_v/\partial z$. It thus characterizes the restoring force that is damping turbulence, and dominates the hyperbolic average in regimes 2 and 3. Also, since $\sigma_w \sim \sqrt{\mathrm{TKE}}$, the two length scales represent the TKE (L_{h2}) versus TPE (L_{h1}) dominated regimes. In fact, L_{h2} emerges naturally from the kinematic heat flux evolution budget equation as an indicator of the relative magnitudes of the gradient production and buoyant destruction terms (see appendix D).

When inserted into the flux model, the Ellison L_{h1} and buoyancy L_{h2} length scales result in the following kinematic heat flux models, respectively [again notice that the resulting models for all regimes are no longer eddy diffusion type closures as indicated by Eqs. (12), and notice that the fluxes for moderate turbulent cases, regimes 2 and 3, scale as $\left(\partial\overline{T}_v/\partial z\right)^{1/2}$; Eq. (12b)] [if one expands the dependence of TPE on $\partial\overline{T}_v/\partial z$, Eq. (12a) suggests no flux dependence on that temperature gradient]:

$$\overline{w'T_v'} = -\alpha_h\sigma_w\sigma_{T_v} = -\alpha_h\sigma_w\sqrt{2\mathrm{TPE}}\left(\frac{\overline{T}_v}{g}\frac{\partial\overline{T}_v}{\partial z}\right)^{1/2}, \tag{12a}$$

$$\overline{w'T_v'} = -(1 - \alpha_h)\frac{\sigma_w^2}{N_{\mathrm{BV}}}\frac{\partial\overline{T}_v}{\partial z} = -(1 - \alpha_h)\sigma_w^2\left(\frac{\overline{T}_v}{g}\frac{\partial\overline{T}_v}{\partial z}\right)^{1/2}. \tag{12b}$$

Both expressions are properly defined if used directly (without computing the mixing length scale first) even in the neutral limit of $\partial\overline{T}_v/\partial z \to 0$, where they both yield zero heat fluxes as expected (but $\partial\overline{T}_v/\partial z$ must be positive, i.e., a stable regime). We note that the TPE is expected to also be zero in that limit, despite the fact that it contains $\partial\overline{T}_v/\partial z$ in its denominator, since the variance in the numerator should also go to zero faster (no TPE can be stored in a field with no temperature gradients).

The empirical constant α_h, determined based on the B09 data and tested unchanged for the B16 data, was found to be $\alpha_h = \alpha_m = 0.35$, the same value for the corresponding momentum model. Another interpretation of α_m that follows from Eq. (10b) and the definition of the correlation coefficient of the horizontal and vertical velocity perturbations, R_{uw}, is that $\alpha_m = -R_{uw}\left(\sigma_u/\overline{U}\right)$, implying that it is the result of the interplay between horizontal turbulence intensity and its correlation with vertical turbulence. Similarly, Eq. (12a) yields $\alpha_h = -R_{T_vw}$, the temperature–vertical velocity correlation coefficient. Given that horizontal turbulence intensity, $I_u = \sigma_u/\overline{U}$, is almost certainly <1 under stable conditions, this interpretation imposes the constraint that both coefficients must have a magnitude < 1 and provides a direct way of measuring them from observations. Furthermore, the similarity of the empirical values of the momentum and heat constants, as well as the fact that in the complementary Eqs. (10a) and (12b) the coefficients that we adopt are $(1 - \alpha_m)$ and $(1 - \alpha_h)$, respectively, suggest that these coefficients also reflect the probabilities of turbulence residing in the different regimes.

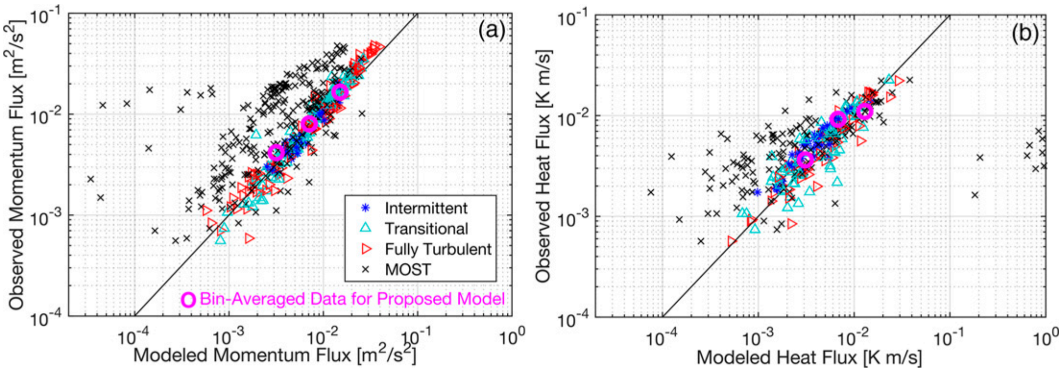

FIG. 9. (a) Momentum flux model and (b) heat flux model evaluation. One-to-one line is shown as a reference (solid black line). Data from both the B09 (1.8 m) and B16 (0.5 m) field campaigns. MOST fluxes are computed using the Businger–Dyer relations (Businger et al. 1971). Bin-averaged data are applied over half decades (if and only if more than 20 points exist within a bin).

c. *Performance of the revised flux model and implementation challenges*

The proposed model is now tested using all statically stable periods from B09 and B16 across all regimes, and the plots depict a strong correlation between the modeled 15-min kinematic fluxes and the observed ones (Fig. 9). The proposed model occasionally overpredicts the fluxes of the transitional and fully turbulent regimes when they are weak, but its performance is much improved relative to MOST. For heat flux, the new model attains a correlation coefficient of 0.61 with observations compared to 0.0047 for MOST, while for momentum fluxes, our model's correlation is 0.94 compared to 0.49 for MOST. Note that MOST requires the measured fluxes to compute the stability corrections and parameterize the fluxes in the present observational analysis, while the proposed model only requires variances and gradients, and thus its parameterized fluxes are not themselves required as input.

MOST has limitations under the stable regime that are corroborated by the analysis here, and the model proposed in Eqs. (10a), (10b), (12a), and (12b) suggests that mixing and fluxes are dominated by vertical turbulence intensity and the bulk velocity (momentum) or bulk static stability (heat) in the moderately turbulent periods, and by local fluctuations in the weakly turbulent periods. Thus, fluxes are not strongly dependent on some externally imposed local vertical gradients as assumed in MOST, but rather, our findings indicate that local gradients are internal variables that shape and are shaped by the turbulence regime and are implicitly accounted for in the expressions of the proposed model. This agrees with Sun et al. (2012), who reported that when the mean wind exceeds a threshold value, i.e., in the moderate turbulent mode (regime 2), large eddies generated by the bulk shear enhance mixing and reduce stratification, $\partial \overline{T}_v/\partial z$, leading to a limit on heat fluxes. This explains why heat fluxes in the fully turbulent regime, that scale as $\left(\partial \overline{T}_v/\partial z\right)^{1/2}$, can be as small as intermittent period heat fluxes (illustrated in Fig. 9).

The variances of the vertical velocity and temperature are the only higher-order statistics needed to model the eddy diffusivity coefficients and fluxes at all model levels away from the surface (mean wind and temperature are also needed). Hence, current NWP models with 1.5- or second-order turbulence closure techniques can use the present formulations, under stable conditions, if they solve the budgets for σ_w^2 and $\sigma_{T_v}^2$ (Mellor and Yamada 1982; Wichmann and Schaller 1986), to which other related budgets, such as the TKE and velocity variance dissipation budgets, can be added. The challenge of formulating surface fluxes at the first model plane above the surface however remains. MOST is almost universally used to compute these surface–air exchanges along with surface roughness lengths, but given its limitation shown here a better alternative is needed. Such an alternative might rely on the present findings, but it needs to explicitly account for surface properties, such as temperature and roughness lengths, to be of practical use in geophysical models.

Another challenge for developing closure models based on the present results is related to the coarse vertical resolution of geophysical models. Our analyses show that intermittent turbulence activity can be drastically different across the limited tower height (~10 m), but all of these elevations will correspond to one grid cell in weather or climate models. The question of how to provide effective vertical averages over such grids, and how to link them to the surface to compute air–surface exchanges (Bou-Zeid et al. 2020), remains an open one. These endeavors, however, must await future investigations.

7. Conclusions

This paper was motivated by three questions related to intermittent turbulence in stable boundary layers, and combined analyses of turbulence data obtained from two field experiments in Utqiaġvik, Alaska, and from direct numerical simulations to seek their answers.

The first question was, "What nondimensional statistical indicators could be used to detect and characterize intermittency?" In section 3, we proposed two such nondimensional indicators and demonstrated that they can effectively identify intermittent periods. The first parameter, I_{weak}, measures turbulence intensity expressed as the first quartile of 10-s box-averaged TKE; it characterizes the weakest turbulence subperiods. The second parameter, CV_e, measures the corresponding standard deviation of TKE, and captures the variability in turbulence activity within the period. Together, these two indicators can distinguish the fully turbulent regimes from the more quiescent ones (though no clearly delineated clusters emerge). They also provide measures for the variability and intensity of the turbulent bursts within the quiescent periods. This result allowed further classification of the quiescent periods into intermittent (where some periods are quasi laminar) and transitional (strong variability in turbulence intensity, but no quasi laminarization). A striking feature of the flow structures in the intermittent periods was their confinement to the lowest air layers, which were effectively decoupled from the flow aloft.

Then, in sections 4 and 5, “What are the origins of the turbulent bursts that enhance mixing and transport under intermittent and transitional regimes?” was explored. This was done using a novel approach of averaging over individual TKE bursts, which were shown to be primarily advected by the mean horizontal wind onto the measurement point, locally generated by mechanical shear production, or lifted from below by turbulent transport. Our findings suggest that even the advected turbulence bursts are most likely associated with height-local but upstream shear produced turbulence. Turbulence intensity and shear generation were found to decrease with height, while the role of upward vertical transport of turbulence as a source of bursting increased. We augmented this analysis with a similar investigation based on DNS data, which broadly confirmed the field analysis conclusions, but also suggested that turbulent pressure transport can play a role in explaining the bursts. Such findings, corroborated by both field data and DNS, confirm the view that bursting events in the stable boundary layer can be triggered by internal mechanisms (bottom-up), but does preclude a simultaneous important role for external triggers. The dominance of internal mechanisms documented here may be a distinct feature of stable ASLs at high latitudes where the diurnal cycles (and hence the LLJs resulting from inertial oscillations) are weaker. The findings may need to be confirmed at locations with more complex topographies that can trigger stronger wave activity, or at midlatitude sites where the LLJ activity and surface heterogeneity may be stronger. Another informative analysis that can build on the present findings would be to analyze the TKE bursts in a Lagrangian framework (here we only used Eulerian analyses) that follows each burst to examine its early genesis and how it strengthens to peak shear production and decays afterward. This is of course only possible using numerical simulations.

Finally, section 6 focused on “How can vertical fluxes across all regimes of stratified turbulence be modeled in a framework commensurate with complexity to existing closure schemes?” Given that conditional analysis of the bursting periods revealed that the transport efficiency is significantly increased relative to the more quiescent periods in the intermittent regime, we sought vertical flux models that give due account to the physical features of the bursts that we elucidated before. An eddy diffusion model was proposed and then examined for all regimes with a focus on intermittent and transitional regimes. However, with many mixing length scales tested, the scales found to provide the highest skill in recovering the measured fluxes convert the model to either a variance or a bulk form. The turbulence closure proposed here is based on the vertical velocity variance, which is found to have the best correlation with the fluxes. The mixing length for momentum is then formed as the hyperbolic average of a w-variance modified shear length scale (L_{m1}) and the classic shear length scale (L_{m2}), which dominate, respectively, in regimes 1 and 2. Similarly, the mixing length scale for heat is the hyperbolic average of the Ellison length scale (L_{h1}) that depends on the turbulent potential energy and the buoyancy length scale (L_{h2}) that relies on the vertical turbulence kinetic energy, i.e., the vertical velocity variance, found to be dominant, respectively, in regimes 1 and 2. These length scales have been proposed previously in the literature, but in this work we offer novel insight and hyperbolic combinations that elucidate the physical processes at play. In addition, the resulting model outperforms MOST significantly, the latter failing to capture the fluxes under stable intermittent regimes, as has been known for quite some time now.

Overall, the findings outline a methodological approach of how to detect intermittency, how turbulent bursts are initiated, and what that detection implies for closure modeling. The methods developed may be as important as the findings, and they can be adopted to investigate intermittency in other flows, locations, and terrain types. Similarly, the new closure model can provide a basis for enhancing turbulence parameterizations for coarser atmospheric models. These models show sensitivity to the parameterized fluxes under stable conditions (Holtslag et al. 2013), and this remains a significant source of bias in weather forecasting and climate projections. Our findings suggest that there are complex features of the stable ABL that are absent from existing turbulence parameterizations (e.g., MOST) and thus a revision of these is overdue, but much work remains needed to translate new closures into effective operational parameterizations at the resolution of weather and climate models.

Acknowledgments. M.A. and E.B.Z. are supported by the Cooperative Institute for Modeling the Earth System at Princeton University under Award NA18OAR4320123 from the National Oceanic and Atmospheric Administration, and by the Andlinger Center for Energy and the Environment at Princeton University. J.D.F. acknowledges the support provided by the National Science Foundation to complete the PHOXMELT field studies (Grant PLR-1417914) to collect the data. We thank Kerri Pratt from the University of Michigan, Paul Shepson from State University of New York Stony Brook, and Jesus Ruiz-Plancart from Penn State University for their contributions to obtaining the turbulence data at Utqiaġvik, Alaska, during 2016. We also thank Ralf Staebler from Environment and Climate Change Canada, Toronto, Canada, who (working with J.D.F.) obtained the OASIS 2009 air turbulence data. The DNS Computing time was provided by the Jülich Supercomputing Centre under the Project HKU24. C.A. acknowledges funding from the European Research Council (ERC) under the European Union’s Horizon 2020 Research and

Innovation Programme (GA 851347). G.K. acknowledges support from NSF-AGS-1644382, NSF-IOS-1754893, and NSF-AGS-2028633. O.C.A. acknowledges support from Brazilian Agencies CNPq and CAPES.

Data availability statement. References are provided to the publicly available Arctic datasets used for observational analysis in the paper. Further data and information can be obtained from coauthor Jose Fuentes (juf15@psu.edu). The raw DNS dataset is massive and not publicly available, but readers can contact coauthor Cedrick Ansorge (cansorge@uni-koeln.de) to obtain the raw data. All derived secondary data discussed and plotted in this paper will be made publicly available with paper publication.

APPENDIX A

Movies

A pseudocolor plot movie from the B16 tower data at all levels depicting the vertical velocity perturbations and the kinematic heat flux was generated. Three periods where the sonic times series at most heights fell within one regime are selected. We produce x–z vertical slices by invoking Taylor's frozen field hypothesis at each height (with its own mean velocity) and locating the tower in the middle of the resulting domain (https://www.dropbox.com/sh/jzh1hwijsmskrqe/AACr5jyCKkK6vEkO0mD7ewYia?dl=0).

APPENDIX B

Bursts of TKE Investigation in Regime 3 (Fully Turbulent)

The analysis focuses here on the identified bursts during fully turbulent periods (regime 3) where a good one-to-one correspondence is observed between the positive tendencies and the largest/dominant TKE term in Eq. (3) (Fig. B1). Similarly, a magnitude intercomparison analysis among the TKE terms reveals the one most responsible for the rise in TKE during each turbulent burst. Figure B1 is a summary of these dominant TKE budget terms explaining the positive tendencies (corresponding to all burst in all periods in Fig. 3 in the fully turbulent regime). In addition to mean flow advection and shear production, streamwise TKE transport by the turbulence is now significant and comparable to vertical turbulent transport. One can also note here that mechanical shear production and mean advection are often much stronger than the corresponding observed tendency in very strong events, which suggests that this generated or advected TKE is partitioned between amplified tendency and transport away or dissipation of TKE.

APPENDIX C

Generalized Closure Formulation

Here we formulate the closure model of section 5 in a Galilean-invariant form, applicable in arbitrary coordinate systems. We continue to assume that the flow is homogeneous in a plane parallel to the Earth surface, where the velocities u and v are in directions x and y, respectively. In the wall-normal direction z, the velocity is w. The wall-normal fluxes of wall-parallel momentum components and heat, invoking the Boussinesq analogy (Momen and Bou-Zeid 2016), are then given by

$$\overline{u'w'} = -K_m \frac{\partial \overline{U}}{\partial z}; \quad \overline{v'w'} = -K_m \frac{\partial \overline{V}}{\partial z}, \tag{C1}$$

$$\overline{w'T_v'} = -K_h \frac{\partial \overline{T}_v}{\partial z}, \tag{C2}$$

and the diffusivities are formulated as in Eq. (8)

$$K_m = \sigma_w L_m, \tag{C3}$$

$$K_h = \sigma_w L_h. \tag{C4}$$

The mixing lengths are then give in terms of the wall-normal gradient of the wall-parallel wind speed $\overline{M} = \sqrt{\overline{U}^2 + \overline{V}^2}$ and the bulk velocity difference between the air and the surface $\Delta\overline{M} = \overline{M}(z) - \overline{M}(z_0)$:

$$L_{m1} = (1 - \alpha_m)\sigma_w \left|\frac{\partial \overline{M}}{\partial z}\right|^{-1}, \tag{C5}$$

$$L_{m2} = \alpha_m |\Delta\overline{M}| \left|\frac{\partial \overline{M}}{\partial z}\right|^{-1}, \tag{C6}$$

$$L_m = \left(\frac{1}{L_{m1}} + \frac{1}{L_{m2}}\right)^{-1}. \tag{C7}$$

This mixing length model requires $\alpha_m \le 1$. The resulting stress models with L_{m1} and L_{m2} are therefore given, respectively, by

$$\begin{aligned} \overline{u'w'} &= -(1 - \alpha_m)\sigma_w^2 \frac{\partial \overline{U}/\partial z}{|\partial \overline{M}/\partial z|}; \\ \overline{v'w'} &= -(1 - \alpha_m)\sigma_w^2 \frac{\partial \overline{V}/\partial z}{|\partial \overline{M}/\partial z|}, \end{aligned} \tag{C8}$$

$$\begin{aligned} \overline{u'w'} &= -\alpha_m \sigma_w |\Delta\overline{M}| \frac{\partial \overline{U}/\partial z}{|\partial \overline{M}/\partial z|}; \\ \overline{v'w'} &= -\alpha_m \sigma_w |\Delta\overline{M}| \frac{\partial \overline{V}/\partial z}{|\partial \overline{M}/\partial z|}. \end{aligned} \tag{C9}$$

For heat, we allow the wall-normal direction not to coincide with the gravity vector; however, we caution against the direct use of the model for katabatic flows since we specifically excluded them from our analysis and since they might involve dynamics that are not captured by this closure model. The Brunt–Väisälä frequency is thus written as $N_{\rm BV} = \left(-g_i \overline{T_v}^{-1} \partial \overline{T}_v / \partial x_i\right)^{1/2}$, where $i = 1, 2, 3$ refers to any of the three coordinate directions and index repetition

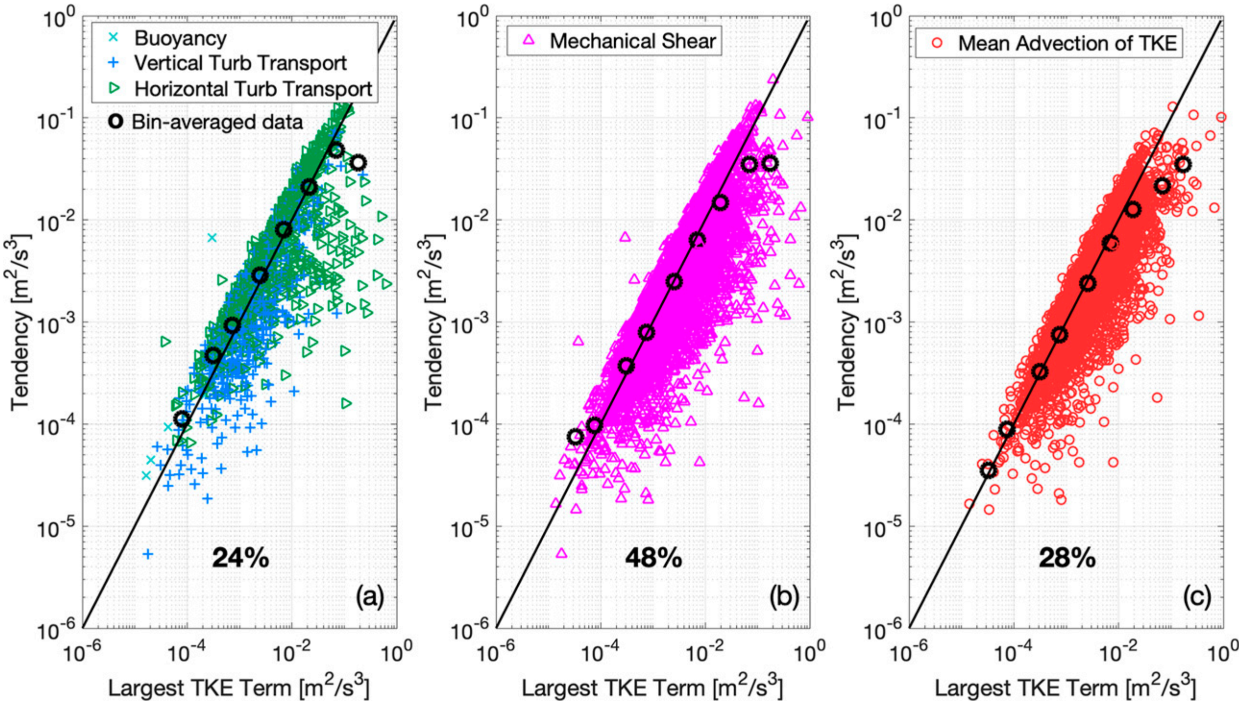

FIG. B1. Bursts' rise origins in regime 3. One-to-one reference (solid black line). Data from the first level (0.5 m) at B16. Bin-averaged data are applied over half decades (if and only if more than 20 points exist within a bin).

implies summation. The gravitational acceleration vector g_i is expressed in the arbitrary coordinate system [in the system used in the main text it would be (0, 0, −9.81) m^2 s^{-1}]. The value of N_{BV} must always remain positive for the stratification to remain stable (within our model's scope). We also maintain the assumption of planar homogeneity (x and y gradients of temperature are zero) implying that $N_{\mathrm{BV}} = \left(-g_3 \overline{T_v}^{-1} \partial \overline{T}_v / \partial z\right)^{1/2}$. The heat mixing lengths are then given by

$$L_{h1} = \alpha_h \sigma_{T_v} \left| \frac{\partial \overline{T}_v}{\partial z} \right|^{-1}, \tag{C10}$$

$$L_{h2} = (1 - \alpha_h) \frac{\sigma_w}{N_{\mathrm{BV}}}, \tag{C11}$$

$$L_h = \left(\frac{1}{L_{h1}} + \frac{1}{L_{h2}} \right)^{-1}, \tag{C12}$$

resulting in the heat fluxes

$$\overline{w' T_v'} = -\alpha_h \sigma_w \sigma_{T_v} \frac{\partial \overline{T}_v / \partial z}{\left| \partial \overline{T}_v / \partial z \right|}, \tag{C13}$$

$$\overline{w' T_v'} = -(1 - \alpha_h) \frac{\sigma_w^2}{N_{\mathrm{BV}}} \frac{\partial \overline{T}_v}{\partial z}. \tag{C14}$$

In a numerical implementation of the model, and if the mixing lengths are to be used directly, the formulation of (C7) and (C12) should be modified to add a third minimum mixing length to prevent model instability in the limit of $\partial \overline{U} / \partial z \rightarrow 0$ (as done, for example, in Huang et al. 2013).

APPENDIX D

Linking L_{h2} to the Heat Flux Budget Equation

A scaling analysis for the relative magnitudes of the gradient production and buoyant destruction terms in the kinematic heat flux evolution budget equation is provided below, elucidating the links of L_{h2} to this budget. We note that the pressure redistribution (or scrambling) term is often on the same order as these two terms in the budget (Shah and Bou-Zeid 2014). So L_{h2} may be encoding the imbalance, rather than the balance, between gradient production and buoyant destruction; an imbalance that then has to be closed by pressure redistribution. Indeed, this imbalance expressed as the ratio between the heat flux buoyant and gradient terms, while not strictly ≈1, was shown by Acevedo et al. (2016) to be the best descriptor of the SBL regime, among the many dimensionless numbers they tested. Physically, this imbalance represents the fraction of the gradient production of downward heat flux in the stable ABL that is compensated for by the (smaller on average) buoyant generation of upward, counter gradient heat flux:

$$-\overline{w'^2}\frac{\partial \overline{T}_v}{\partial z} + \overline{T_v'^2}\frac{g}{\overline{T}_v} = 0$$

$$\Rightarrow \overline{T_v'^2} = \overline{w'^2}\frac{\partial \overline{T}_v}{\partial z}\frac{\overline{T}_v}{g} \sim L_{h2}^2\left(\frac{\partial \overline{T}_v}{\partial z}\right)^2$$

$$\Rightarrow L_{h2}^2 \sim \sigma_w^2\left(\frac{\partial \overline{T}_v}{\partial z}\right)^{-1}\frac{\overline{T}_v}{g}$$

$$\Rightarrow L_{h2} \sim \sigma_w\left[\left(\frac{\partial \overline{T}_v}{\partial z}\right)^{-1}\frac{\overline{T}_v}{g}\right]^{1/2} = \frac{\sigma_w}{N_{\mathrm{BV}}}.$$

REFERENCES

Acevedo, O. C., and D. R. Fitzjarrald, 2003: In the core of the night—Effects of intermittent mixing on a horizontally heterogeneous surface. *Bound.-Layer Meteor.*, **106**, 1–33, https://doi.org/10.1023/A:1020824109575.

——, F. D. Costa, P. E. S. Oliveira, F. S. Puhales, G. A. Degrazia, and D. R. Roberti, 2013: The influence of submeso processes on stable boundary layer similarity relationships. *J. Atmos. Sci.*, **71**, 207–225, https://doi.org/10.1175/JAS-D-13-0131.1.

——, L. Mahrt, F. S. Puhales, F. D. Costa, L. E. Medeiros, and G. A. Degrazia, 2016: Contrasting structures between the decoupled and coupled states of the stable boundary layer. *Quart. J. Roy. Meteor. Soc.*, **142**, 693–702, https://doi.org/10.1002/qj.2693.

Anfossi, D., D. Oettl, G. Degrazia, and A. Goulart, 2005: An analysis of sonic anemometer observations in low wind speed conditions. *Bound.-Layer Meteor.*, **114**, 179–203, https://doi.org/10.1007/s10546-004-1984-4.

Ansorge, C., and J. P. Mellado, 2014: Global intermittency and collapsing turbulence in the stratified planetary boundary layer. *Bound.-Layer Meteor.*, **153**, 89–116, https://doi.org/10.1007/s10546-014-9941-3.

——, and ——, 2016: Analyses of external and global intermittency in the logarithmic layer of Ekman flow. *J. Fluid Mech.*, **805**, 611–635, https://doi.org/10.1017/jfm.2016.534.

Antonia, R. A., 1981: Conditional sampling in turbulence measurement. *Annu. Rev. Fluid Mech.*, **13**, 131–156, https://doi.org/10.1146/annurev.fl.13.010181.001023.

Ayet, A., G. G. Katul, A. D. Bragg, and J. L. Redelsperger, 2020: Scalewise return-to-isotropy in stratified boundary layer flows. *J. Geophys. Res. Atmos.*, **125**, e2020JD032732, https://doi.org/10.1029/2020JD032732.

Banta, R. M., L. Mahrt, D. Vickers, J. Sun, B. B. Balsley, Y. L. Pichugina, and E. J. Williams, 2007: The very stable boundary layer on nights with weak low-level jets. *J. Atmos. Sci.*, **64**, 3068–3090, https://doi.org/10.1175/JAS4002.1.

Bottenheim, J. W., R. M. Staebler, and J. D. Fuentes, 2013: OASIS-CANADA Barrow-09 Tower Study: Atmospheric micrometeorology study during the international OASIS-09 campaign near Barrow, Alaska. EUDAT, accessed 1 April 2009, http://b2find.eudat.eu/dataset/638aab64-7fb1-5d04-b320-cb05d373c4c2.

Bou-Zeid, E., W. Anderson, G. G. Katul, and L. Mahrt, 2020: The persistent challenge of surface heterogeneity in boundary-layer meteorology: A review. *Bound.-Layer Meteor.*, **177**, 227–245, https://doi.org/10.1007/s10546-020-00551-8.

Businger, J. A., J. C. Wyngaard, Y. Izumi, and E. F. Bradley, 1971: Flux–profile relationships in the atmospheric surface layer. *J. Atmos. Sci.*, **28**, 181–189, https://doi.org/10.1175/1520-0469(1971)028<0181:FPRITA>2.0.CO;2.

Cava, D., U. Giostra, M. Siqueira, and G. G. Katul, 2004: Organised motion and radiative perturbations in the nocturnal canopy sublayer above an even-aged pine forest. *Bound.-Layer Meteor.*, **112**, 129–157, https://doi.org/10.1023/B:BOUN.0000020160.28184.a0.

——, L. Mortarini, U. Giostra, O. Acevedo, and G. G. Katul, 2019: Submeso motions and intermittent turbulence across a nocturnal low-level jet: A self-organized criticality analogy. *Bound.-Layer Meteor.*, **172**, 17–43, https://doi.org/10.1007/s10546-019-00441-8.

Chamecki, M., N. L. Dias, S. T. Salesky, and Y. Pan, 2017: Scaling laws for the longitudinal structure function in the atmospheric surface layer. *J. Atmos. Sci.*, **74**, 1127–1147, https://doi.org/10.1175/JAS-D-16-0228.1.

Costa, F. D., O. C. Acevedo, J. C. M. Mombach, and G. A. Degrazia, 2011: A simplified model for intermittent turbulence in the nocturnal boundary layer. *J. Atmos. Sci.*, **68**, 1714–1729, https://doi.org/10.1175/2011JAS3655.1.

Coulter, R. L., and J. C. Doran, 2002: Spatial and temporal occurrences of intermittent turbulence during CASES-99. *Bound.-Layer Meteor.*, **105**, 329–349, https://doi.org/10.1023/A:1019993703820.

Cuxart, J., M. Jimenez, and M. A. Jiménez, 2007: Mixing processes in a nocturnal low-level jet: An LES study. *J. Atmos. Sci.*, **64**, 1666–1679, https://doi.org/10.1175/JAS3903.1.

Deusebio, E., C. P. Caulfield, and J. R. Taylor, 2015: The intermittency boundary in stratified plane Couette flow. *J. Fluid Mech.*, **781**, 298–329, https://doi.org/10.1017/jfm.2015.497.

Donda, J. M. M., I. G. S. Van Hooijdonk, A. F. Moene, H. J. J. Jonker, G. J. F. van Heijst, H. J. H. Clercx, and B. H. H. Van de Wiel, 2015: Collapse of turbulence in stably stratified channel flow: A transient phenomenon. *Quart. J. Roy. Meteor. Soc.*, **141**, 2137–2147, https://doi.org/10.1002/qj.2511.

Du, Y., and R. Rotunno, 2014: A simple analytical model of the nocturnal low-level jet over the Great Plains of the United States. *J. Atmos. Sci.*, **71**, 3674–3683, https://doi.org/10.1175/JAS-D-14-0060.1.

Durbin, P. A., 2018: Some recent developments in turbulence closure modeling. *Annu. Rev. Fluid Mech.*, **50**, 77–103, https://doi.org/10.1146/annurev-fluid-122316-045020.

Durst, C. S., 1933: The breakdown of steep wind gradients in inversions. *Quart. J. Roy. Meteor. Soc.*, **59**, 131–136, https://doi.org/10.1002/qj.49705924906.

Ellison, T. H., 1957: Turbulent transport of heat and momentum from an infinite rough plane. *J. Fluid Mech.*, **2**, 456–466, https://doi.org/10.1017/S0022112057000269.

Fernando, H. S., 2005: Turbulent patches in a stratified shear flow. *Phys. Fluids*, **15**, 3164, https://doi.org/10.1063/1.1602076.

——, and J. C. Weil, 2010: Whither the stable boundary layer? A shift in the research agenda. *Bull. Amer. Meteor. Soc.*, **91**, 1475–1484, https://doi.org/10.1175/2010BAMS2770.1.

Ghannam, K., and E. Bou-Zeid, 2020: Baroclinicity and directional shear explain departures from the logarithmic wind profile. *Quart. J. Roy. Meteor. Soc.*, **147**, 443–464, https://doi.org/10.1002/qj.3927.

Grachev, A. A., E. L. Andreas, C. W. Fairall, P. S. Guest, and P. O. G. Persson, 2014: Similarity theory based on the Dougherty–Ozmidov length scale. *Quart. J. Roy. Meteor. Soc.*, **141**, 1845–1856, https://doi.org/10.1002/qj.2488.

Holtslag, A. A. M., and Coauthors, 2013: Stable atmospheric boundary layers and diurnal cycles: Challenges for weather and climate models. *Bull. Amer. Meteor. Soc.*, **94**, 1691–1706, https://doi.org/10.1175/BAMS-D-11-00187.1.

Huang, J., and E. Bou-Zeid, 2013: Turbulence and vertical fluxes in the stable atmospheric boundary layer. Part I: A large-eddy simulation study. *J. Atmos. Sci.*, **70**, 1513–1527, https://doi.org/10.1175/JAS-D-12-0167.1.

——, ——, and J. C. Golaz, 2013: Turbulence and vertical fluxes in the stable atmospheric boundary layer. Part II: A novel mixing-length model. *J. Atmos. Sci.*, **70**, 1528–1542, https://doi.org/10.1175/JAS-D-12-0168.1.

Katul, G. G., A. Porporato, S. Shah, and E. Bou-Zeid, 2014: Two phenomenological constants explain similarity laws in stably stratified turbulence. *Phys. Rev. E*, **89**, 023007, https://doi.org/10.1103/PhysRevE.89.023007.

Lan, C., H. Liu, G. G. Katul, D. Li, and D. Finn, 2019: Large eddies regulate turbulent flux gradients in coupled stable boundary layers. *Geophys. Res. Lett.*, **46**, 6090–6100, https://doi.org/10.1029/2019GL082228.

Lloyd, S. P., 1982: Least squares quantization in PCM. *IEEE Trans. Inf. Theory*, **28**, 129–137, https://doi.org/10.1109/TIT.1982.1056489.

Mahrt, L., 1998: Nocturnal boundary-layer regimes. *Bound.-Layer Meteor.*, **88**, 255–278, https://doi.org/10.1023/A:1001171313493.

——, 1999: Stratified atmospheric boundary layers. *Bound.-Layer Meteor.*, **90**, 375–396, https://doi.org/10.1023/A:1001765727956.

——, and D. Vickers, 2006: Extremely weak mixing in stable conditions. *Bound.-Layer Meteor.*, **119**, 19–39, https://doi.org/10.1007/s10546-005-9017-5.

——, and E. Bou-Zeid, 2020: Non-stationary boundary layers. *Bound.-Layer Meteor.*, **177**, 189–204, https://doi.org/10.1007/s10546-020-00533-w.

——, C. Thomas, S. Richardson, N. Seaman, D. Stauffer, and M. Zeeman, 2013: Non-stationary generation of weak turbulence for very stable and weak-wind conditions. *Bound.-Layer Meteor.*, **147**, 179–199, https://doi.org/10.1007/s10546-012-9782-x.

——, J. Sun, and D. Stauffer, 2015: Dependence of turbulent velocities on wind speed and stratification. *Bound.-Layer Meteor.*, **155**, 55–71, https://doi.org/10.1007/s10546-014-9992-5.

Mellor, G. L., and T. Yamada, 1982: Development of a turbulence closure model for geophysical fluid problems. *Rev. Geophys.*, **20**, 851–875, https://doi.org/10.1029/RG020i004p00851.

Momen, M., and E. Bou-Zeid, 2016: Large-eddy simulations and damped-oscillator models of the unsteady Ekman boundary layer. *J. Atmos. Sci.*, **73**, 25–40, https://doi.org/10.1175/JAS-D-15-0038.1.

Muschinski, A., and P. P. Sullivan, 2013: Using large-eddy simulation to investigate intermittency fluxes of clear-air radar reflectivity in the atmospheric boundary layer. *IEEE Antennas and Propagation Society International Symp.*, Orlando, FL, IEEE, 2321–2322, https://doi.org/10.1109/APS.2013.6711819.

——, R. G. Frehlich, and B. B. Balsley, 2004: Small-scale and large-scale intermittency in the nocturnal boundary layer and the residual layer. *J. Fluid Mech.*, **515**, 319–351, https://doi.org/10.1017/S0022112004000412.

Nappo, C. J., 1991: Sporadic breakdowns of stability in the PBL over simple and complex terrain. *Bound.-Layer Meteor.*, **54**, 69–87, https://doi.org/10.1007/BF00119413.

Narasimha, R., and K. R. Sreenivasan, 1973: Relaminarization in highly accelerated turbulent boundary layers. *J. Fluid Mech.*, **61**, 417–447, https://doi.org/10.1017/S0022112073000790.

Nieuwstadt, F. T. M., 1984: The turbulent structure of the stable, nocturnal boundary layer. *J. Atmos. Sci.*, **41**, 2202–2216, https://doi.org/10.1175/1520-0469(1984)041<2202:TTSOTS>2.0.CO;2.

Pardyjak, E. R., P. Monti, and H. J. S. Fernando, 2002: Flux Richardson number measurements in stable atmospheric shear flows. *J. Fluid Mech.*, **459**, 307–316, https://doi.org/10.1017/S0022112002008406.

Perrie, W., and Coauthors, 2012: Selected topics in Arctic atmosphere and climate. *Climatic Change*, **115**, 35–58, https://doi.org/10.1007/s10584-012-0493-6.

Persson, P. O. G., 2003: Measurements near the atmospheric surface flux group tower at SHEBA: Near-surface conditions and surface energy budget. *J. Geophys. Res.*, **107**, 8045, https://doi.org/10.1029/2000JC000705.

Poggi, D., A. Porporato, L. Ridolfi, J. D. Albertson, and G. G. Katul, 2004: The effect of vegetation density on canopy sublayer turbulence. *Bound.-Layer Meteor.*, **111**, 565–587, https://doi.org/10.1023/B:BOUN.0000016576.05621.73.

Pope, S. B., 2000: *Turbulent Flows*. Cambridge University Press, 806 pp.

Richter-Menge, J., J. E. Overland, J. T. Mathis, and E. Osborne, 2017: Arctic report card: Update for 2017. National Oceanic and Atmospheric Administration, https://www.arctic.noaa.gov/Report-Card/Report-Card-2017.

Rorai, C., P. D. Mininni, and A. Pouquet, 2014: Turbulence comes in bursts in stably stratified flows. *Phys. Rev. E*, **89**, 043002, https://doi.org/10.1103/PhysRevE.89.043002.

Ruiz-Plancarte, J., J. D. Fuentes, and S. Thanekar, 2016: Air turbulence data over the Barrow Environmental Observatory, 2016. Arctic Data Center, accessed 19 December 2017, https://doi.org/10.18739/A2R20RW3W.

Shah, S. K., and E. Bou-Zeid, 2014: Direct numerical simulations of turbulent Ekman layers with increasing static stability: Modifications to the bulk structure and second-order statistics. *J. Fluid Mech.*, **760**, 494–539, https://doi.org/10.1017/jfm.2014.597.

——, and ——, 2019: Rate of decay of turbulent kinetic energy in abruptly stabilized Ekman boundary layers. *Phys. Rev. Fluids*, **4**, 074602, https://doi.org/10.1103/PhysRevFluids.4.074602.

Shaw, R. H., 1977: Secondary wind speed maxima inside plant canopies. *J. Appl. Meteor. Climatol.*, **16**, 514–521, https://doi.org/10.1175/1520-0450(1977)016<0514:SWSMIP>2.0.CO;2.

Sorbjan, Z., 2010: Gradient-based scales and similarity laws in the stable boundary layer. *Quart. J. Roy. Meteor. Soc.*, **136**, 1243–1254, https://doi.org/10.1002/qj.638.

Staebler, R. M., J. D. Fuentes, and J. W. Bottenheim, 2009: The role of surface and boundary layer dynamics in Arctic ozone depletion episodes. *Eos, Trans. Amer. Geophys. Union*, **90** (Fall Meeting Suppl.), Abstract A24B-05.

Stensrud, D. J., 2007: *Parameterization Schemes: Keys to Understanding Numerical Weather Prediction Models*. Cambridge University Press, 480 pp.

Strong, C., J. D. Fuentes, R. E. Davis, and J. W. Bottenheim, 2002: Thermodynamic attributes of Arctic boundary layer ozone depletion. *Atmos. Environ.*, **36**, 2641–2652, https://doi.org/10.1016/S1352-2310(02)00114-0.

Stull, R. B., 1973: Inversion rise model based on penetrative convection. *J. Atmos. Sci.*, **30**, 1092–1099, https://doi.org/10.1175/1520-0469(1973)030<1092:IRMBOP>2.0.CO;2.

——, 2008: *An Introduction to Boundary Layer Meteorology*. Springer, 684 pp.

Sun, J., and Coauthors, 2002: Intermittent turbulence associated with a density current passage in the stable boundary layer. *Bound.-Layer Meteor.*, **105**, 199–219, https://doi.org/10.1023/A:1019969131774.

——, and Coauthors, 2004: Atmospheric disturbances that generate intermittent turbulence in nocturnal boundary layers. *Bound.-Layer Meteor.*, **110**, 255–279, https://doi.org/10.1023/A:1026097926169.

——, L. Mahrt, R. M. Banta, and Y. L. Pichugina, 2012: Turbulence regimes and turbulence intermittency in the stable boundary layer during CASES-99. *J. Atmos. Sci.*, **69**, 338–351, https://doi.org/10.1175/JAS-D-11-082.1.

Svensson, G., and A. A. M. Holtslag, 2009: Analysis of model results for the turning of the wind and related momentum fluxes in the stable boundary layer. *Bound.-Layer Meteor.*, **132**, 261–277, https://doi.org/10.1007/s10546-009-9395-1.

Taylor, G. I., 1922: Diffusion by continuous movements. *Proc. London Math. Soc.*, **s2-20**, 196–212, https://doi.org/10.1112/plms/s2-20.1.196.

Van der Linden, S. J. A., B. J. H. Van de Wiel, I. Petenko, C. C. van Heerwaarden, P. Baas, and H. J. J. Jonker, 2020: A Businger mechanism for intermittent bursting in the stable boundary layer. *J. Atmos. Sci.*, **77**, 3343–3360, https://doi.org/10.1175/JAS-D-19-0309.1.

Van de Wiel, B. J. H., A. F. Moene, O. K. Hartogensis, H. A. R. de Bruin, and A. A. M. Holtslag, 2003: Intermittent turbulence in the stable boundary layer over land. Part III: A classification for observations during CASES-99. *J. Atmos. Sci.*, **60**, 2509–2522, https://doi.org/10.1175/1520-0469(2003)060<2509:ITITSB>2.0.CO;2.

——, ——, H. J. J. Jonker, P. Baas, S. Basu, J. J. M. Donda, J. Sun, and A. A. M. Holtslag, 2012: The minimum wind speed for sustainable turbulence in the nocturnal boundary layer. *J. Atmos. Sci.*, **69**, 3116–3127, https://doi.org/10.1175/JAS-D-12-0107.1.

Van Hooijdonk, I. G. S., H. J. H. Clercx, C. Ansorge, A. F. Moene, and B. J. H. Van de Wiel, 2018: Parameters for the collapse of turbulence in the stratified plane Couette flow. *J. Atmos. Sci.*, **75**, 3211–3231, https://doi.org/10.1175/JAS-D-17-0335.1.

Vercauteren, N., and R. Klein, 2015: A clustering method to characterize intermittent bursts of turbulence and interaction with submeso motions in the stable boundary layer. *J. Atmos. Sci.*, **72**, 1504–1517, https://doi.org/10.1175/JAS-D-14-0115.1.

——, V. Boyko, A. Kaiser, and D. Belusic, 2019: Statistical investigation of flow structures in different regimes of the stable boundary layer. *Bound.-Layer Meteor.*, **173**, 143–164, https://doi.org/10.1007/s10546-019-00464-1.

Weil, J. C., 2011: Stable boundary layer modeling for air quality applications. *Air Pollution Modeling and its Application XXI*, D. G. Steyn and S. T. Castelli, Eds., Springer, 57–61.

Wendisch, M., and Coauthors, 2017: Understanding causes and effects of rapid warming in the Arctic. *Eos, Trans. Amer. Geophys. Union*, **98**, https://doi.org/10.1029/2017EO064803.

Wichmann, M., and E. Schaller, 1986: On the determination of the closure parameters in higher-order closure models. *Bound.-Layer Meteor.*, **37**, 323–341, https://doi.org/10.1007/BF00117481.

Williams, O., T. Hohman, T. Van Buren, E. Bou-Zeid, and A. J. Smits, 2017: The effect of stable thermal stratification on turbulent boundary layer statistics. *J. Fluid Mech.*, **812**, 1039–1075, https://doi.org/10.1017/jfm.2016.781.

Wyngaard, J. C., N. Seaman, S. J. Kimmel, M. Otte, X. Di, and K. E. Gilbert, 2001: Concepts, observations, and simulation of refractive index turbulence in the lower atmosphere. *Radio Sci.*, **36**, 643–669, https://doi.org/10.1029/2000RS002380.

Zeman, O., and H. Tennekes, 1977: Parameterization of the turbulent energy budget at the top of the daytime atmospheric boundary layer. *J. Atmos. Sci.*, **34**, 111–123, https://doi.org/10.1175/1520-0469(1977)034<0111:POTTEB>2.0.CO;2.

Zilitinkevich, S. S., and I. N. Esau, 2007: Similarity theory and calculation of turbulent fluxes at the surface for the stably stratified atmospheric boundary layer. *Atmospheric Boundary Layers*, A. Baklanov and B. Grisogono, Eds., Springer, 37–49.

——, T. Elperin, N. Kleeorin, I. Rogachevskii, and I. Esau, 2013: A hierarchy of energy- and flux-budget (EFB) turbulence closure models for stably-stratified geophysical flows. *Bound.-Layer Meteor.*, **146**, 341–373, https://doi.org/10.1007/s10546-012-9768-8.